Draping of Cluster Magnetic Fields over Bullets and Bubbles – Morphology and Dynamic Effects

L. J. Dursi and C. Pfrommer

Canadian Institute for Theoretical Astrophysics, University of Toronto, Toronto, ON, M5S 3H8, Canada

ljdursi@cita.utoronto.ca, pfrommer@cita.utoronto.ca

ABSTRACT

High-resolution X-ray observations have revealed cavities and 'cold fronts' with sharp edges in temperature, density, and metallicity within galaxy clusters. Their presence poses a puzzle since these features are not expected to be hydrodynamically stable, or to remain sharp in the presence of diffusion. However, a moving core or bubble in even a very weakly magnetized plasma necessarily sweeps up enough magnetic field to build up a dynamically important sheath around the object; the layer's strength is set by a competition between 'plowing up' of field and field lines slipping around the core, and to first order depends only on the ram pressure seen by the moving object. We show that a two-dimensional approach to the problem as suggested in previous literature is quite generally not possible as the field cannot slip around. In three dimensions, we show with analytic arguments and in numerical experiments, that this magnetic layer modifies the dynamics of a plunging core, greatly modifies the effects of hydrodynamic instabilities on, and thus mixing of, the core, modifies the geometry of stripped material, and even slows the fall of the core through magnetic tension. We derive an expression for the maximum magnetic field strength and the thickness of the layer, as well as for the opening angle of the magnetic wake. The morphology of the magnetic draping layer implies the suppression of thermal conduction across the layer, thus conserving strong temperature gradients over the contact surface. The intermittent amplification of the magnetic field as well as the injection of MHD turbulence in the wake of the core is identified to be due to vorticity generation within the magnetic draping layer. These results have important consequences for understanding the physical properties and the complex gasdynamical processes of the intra-cluster medium, and apply quite generally to motions through other magnetized environments, *e.g.* the ISM.

Subject headings: hydrodynamics — magnetic fields — MHD — turbulence — galaxies: clusters: general — diffusion

1. INTRODUCTION

Recent observations of very sharp 'cold fronts' in galaxy clusters raise unanswered questions in the hydrodynamics of galaxy clusters (see for instance the review of Markevitch and Vikhlinin 2007), for such abrupt transitions are not expected to be stable against either hydrodynamical motions or diffusion for extended periods of time.

It has been known for some decades in the space science community that an object moving super-Alfvénically in a magnetized medium can very rapidly sweep up a significant magnetic layer which is then 'draped' over the projectile (*e.g.*, Bernikov and Semenov 1980). For concreteness in discussing the process, we show in Fig. 1 a picture of this mechanism taken from one of our simulations, which will be described in more detail in later sections.

There has been significant interest in applying this idea of magnetic draping in galaxy clusters (*e.g.*, Vikhlinin et al. 2001; Lyutikov 2006; Asai et al. 2004, 2005, 2006) as such a magnetic field could naturally inhibit thermal conduction across a front (*e.g.*, Ettori and Fabian 2000) allowing it to remain sharp over dynamically long times. Although such draping has been explored in the past, in the space sciences the resulting dynamics is relatively simpler, as generally the object being draped is a solid body, with little interior dynamics of its own. However, in the case of for instance a merger of gas-rich clusters, the hydrodynamics of the draped plunging core can also be modified, with the strong magnetic layer providing some stabilization against instabilities that would otherwise occur (Dursi 2007).

The effect of a strong draped magnetic layer could be even greater for underdense objects, such as for bubbles moving through the intercluster medium, as seen at the centers of many cool-core clusters (*e.g.*, McNamara et al. 2005; Bîrzan et al. 2004). In this case, the bubble would be quickly disrupted on rising absent some sort of support (*e.g.*, Robinson et al. 2004). However, the draping of a pre-existing magnetic field may strongly alter the dynamics and suppress hydrodynamic instabilities, as seen recently in simulations (Ruszkowski et al. 2007b). The morphology of the draped magnetic field may be able to suppress transport processes across the bubble interface such as cosmic ray diffusion and heat conduction. This has important consequences for cosmic ray confinement in these buoyantly rising bubbles and may explain re-energized radio 'relic' sources, broad central abundance profiles of clusters, and the excitation of the Hα line in filaments trailing behind bubbles (Ruszkowski et al. 2007a). Although the analytics and simulations we discuss here focus on the case of an overdense 'core' moving in an external field, we expect the basic magnetic dynamics to also extend to the case of an underdense bubble probably depending on the magnetic energy density of the plasma.

Because we are interested here in the fundamentals of a basic process — that of the draping of a field around an object and the resulting hydrodynamical effect on the object and its interaction

with the external medium — we consider for this paper, in both our analytic and computational work, the simplest possible case; an overdense, non-self-gravitating 'blob' moving through a quiescent medium with a magnetic field uniform on the scales considered. (The term we will use for this blob will depend on the situation; when discussing astrophysical implications, we will speak of 'cores' or 'bullets', depending on the circumstances, or 'bubbles' for underdense regions; for the case of our numerical simulations, we will refer to 'projectiles', as the overdense fluid in the simulations differs in structure from cores or bullets in lacking self gravity; in our analytic work where the blob is a rigid sphere, we will refer to the blob as a sphere or spherical body.)

We further consider the case of the object moving subsonically; while the case of supersonic motion is interesting and highly relevant, we anticipate that in the usual case where the bow shock is well separated from the magnetic layer – that is where the standoff distance $\Delta \approx \frac{\rho_0}{\rho_s} R \sim R$, (where R is the radius of the core, ρ_0 is the ambient density, and ρ_s is the shocked density) is much greater than the magnetic layer thickness $l \approx \mathcal{M}_A^{-2} R \ll R$, (where l is the approximate magnetized layer thickness and $\mathcal{M}_A$ the alfvénic Mach number, as discussed in more detail in the next section) that the arguments here will also hold, so we save the more complicated geometry and larger parameter space of the compressible case for future work.

In §2 we give an overview of the physics of draping, putting our work in the context of previous results; in §3 we describe our analytic and computational approaches; in §4 we compare the results of our two approaches, and from the understanding gained there in §5 we describe characteristics of draping; we discuss the effect of instabilities in §6, consider the limitations of our results and consider applying them to later times in §7, and finally conclude in §8.

2. GENERAL PHYSICS OF MAGNETIC DRAPING

Previous work (*e.g.*, Bernikov and Semenov 1980; Lyutikov 2006) has looked at the basic picture of magnetic draping in a simplified way in some detail; we summarize some of their key results as well as our new insight into this problem here. In these works, the known potential flow around a solid sphere is taken as an input, and a purely kinematic magnetic field, uniform and perpendicular to the direction of motion, is added. The derivation of Bernikov and Semenov (1980) is clarified, and a novel set of useful approximations for the resulting field near the solid sphere are given, in Appendix A.

Because in this case the flow falls quickly to zero at the surface of the moving sphere, magnetic field rapidly 'builds up' around the projectile, and in the kinematic limit eventually becomes infinite. The high degree of symmetry along the stagnation line (the axis of symmetry of the object pointing in the direction of motion) greatly simplifies the mathematics, and as shown in for
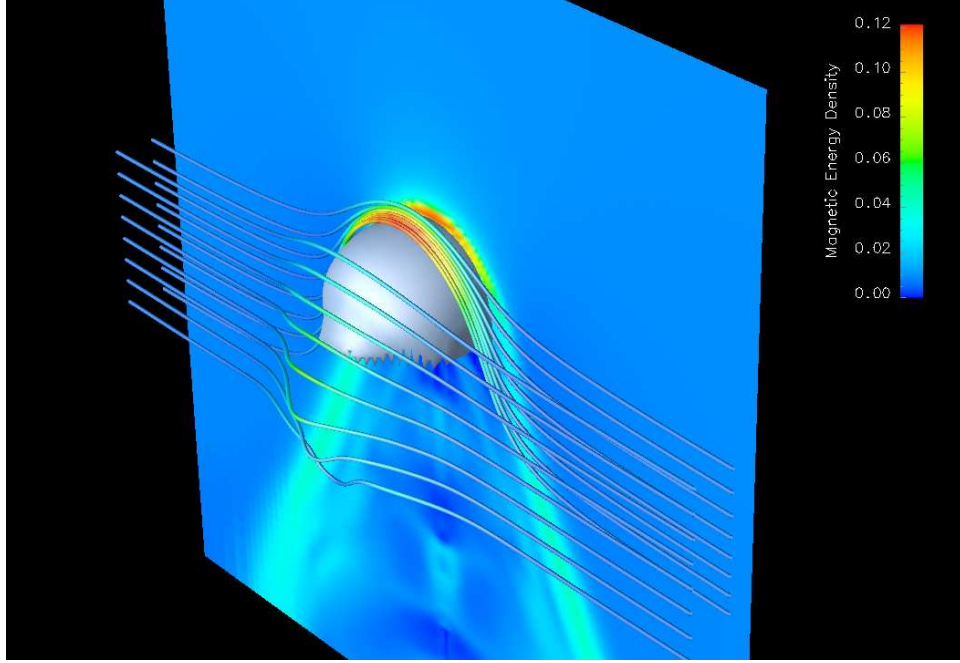
Fig. 1.— A rendering of one of the three-dimensional simulations (referred to as Run F later in this work) performed for this work, discussed in more detail in later sections but included here to illustrate the physical picture. An overdense projectile is sent through a uniformly magnetized medium, sweeping up magnetic field ahead of it. Plotted is a density isosurface, corresponding to the mean density of the bullet, and some fiducial magnetic field lines. The cut-plane is coloured by magnetic energy density, as are the field lines. The magnetic field is 'draped' into a thin layer forming a bow wave, leaving turbulence in a wake behind the bullet. Magnetic field lines pile up along the stagnation line of this initially axisymmetric bullet, while in the plane perpendicular to the initial field, the field lines can slip around the bullet.

instance Lyutikov (2006), the magnetic field strength directly along the stagnation line is given by

$$\frac{|B|}{\rho} = \frac{B_0}{\rho_0} \frac{1}{\sqrt{1 - \left(\frac{R}{R+s}\right)^3}} \tag{1}$$

where B_0 is the ambient magnetic field, ρ_0 is the ambient density, R is the radius of the solid sphere projectile, and s is the distance along the stagnation line from the surface of the sphere.

The analytic works cited, and presented here, considered purely incompressible flow; for our simulations, we consider only very modest compressibility, with projectile motions through the ambient fluid quite subsonic, so it suffices for the moment to consider in the external medium $\rho = \rho_0$. The fluid here is further considered to be infinitely conducting; however, the buildup of magnetic field without a corresponding buildup of mass does not violate the 'flux-freezing' condi-

– 5 –

Fig. 2.— Interactive 3D version of Figure 1 above, following Barnes and Fluke (2007).

tion, as shown in the cartoon Fig. 3 as incoming fluid elements are 'squished' along the sides of the incoming sphere, so that the magnetic flux coming out the sides of the fluid element remains constant, even as the concentration of field lines builds up along the stagnation line. Further increase in magnetic energy comes from the stretching of field lines in the direction of motion of the core.

In reality, of course, the magnetic field does back-react onto the flow, and the kinematic potential flow solution fails for two reasons – buildup of a strong magnetic field layer (which violates the kinematic assumption) and creation of vorticity (in conflict with the potential flow assumptions).

The magnetic field should exert a significant back-reaction when the resulting magnetic pressure is comparable to the ram pressure of the incoming material: $B^2/8\pi \sim \rho_0 u^2$, where u is the speed of the core through the quiescent ambient fluid. The first place this will happen is along the
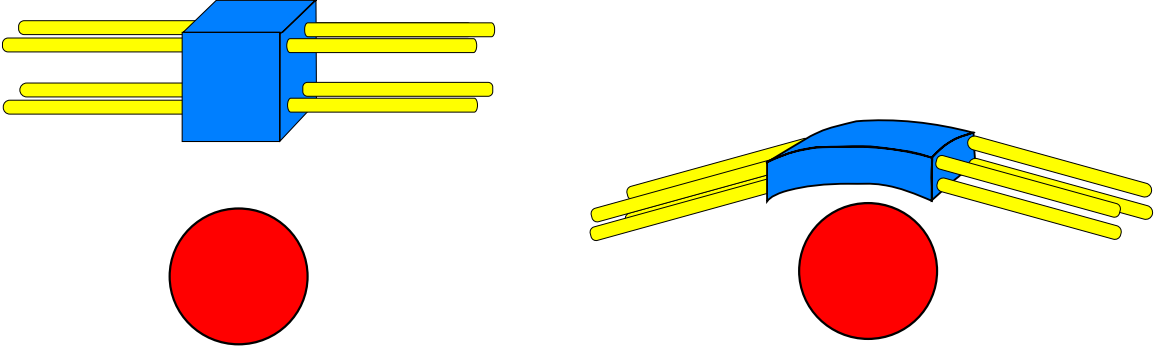
Fig. 3.— A cartoon showing the distortion of incoming fluid elements and stretching of field lines as a red spherical projectile moves upwards through the ambient medium.

stagnation line, which by symmetry will be the location of the largest magnetic energy density. The layer of magnetic field with this magnitude is expected (from Eq. 1 and assuming $l \ll R$) to be of thickness

$$l = \frac{1}{6\alpha \mathcal{M}_A^2} R \qquad (2)$$

where $\mathcal{M}_A = u/v_A$ is the Alfvénic Mach number of the core, $v_A^2 = B_0^2/4\pi\rho_0$ is the ambient Alfvén speed, and α is the constant of proportionality describing the maximum magnetic pressure in units of the incoming ram pressure, $B_{\max}^2/8\pi = \alpha\rho_0 u^2$. We will see that $\alpha \approx 2$ and fiducial values for the situations considered here will involve $\mathcal{M}_A^2 \approx 3$, so that a typical value for l will be approximately $R/36$. Even such a very thin layer can have important effects, both in terms of suppressing thermal conduction (Ettori and Fabian 2000) and hydrodynamic instabilities (Dursi 2007).

It should be noted here that when we use the Alfvénic Mach number $\mathcal{M}_A$ through this work it should really be considered a dimensionless ratio of ram pressure to magnetic pressure ($\mathcal{M}_A^2 = \rho_0 u^2/(2P_{B_0})$), or at the least, some caution should be used when interpreting it as a ratio of velocities (u/v_A) as the velocities are oriented in different directions; in the work presented here, the velocity of the draped object will always be completely orthogonal to the ambient direction of propagation of Alfvén waves. Thus there is an important sense in which our projectiles are always (infinitely) super-Alfvénic, which is not captured in the ratio $\mathcal{M}_A$.

Sweeping up such a magnetic field will occur on a timescale $t/t_c \sim \sqrt{\alpha}(l/R)\mathcal{M}_A \sim (\sqrt{\alpha}\mathcal{M}_A)^{-1}$, where $t_c = 2R/u$ is the projectile's own crossing time. This result means that, because the magnetic layer is very thin, a strong field can be built up extremely quickly. Crucially, particularly for the propagation of bubbles, the sweep-up time can be significantly smaller than a single crossing time; this is relevant because a purely hydrodynamic bubble will generally self-disrupt into a torus, or smaller fragments in a turbulent medium, in on order a crossing time (Robinson et al. 2004; Pavlovski et al. 2007).
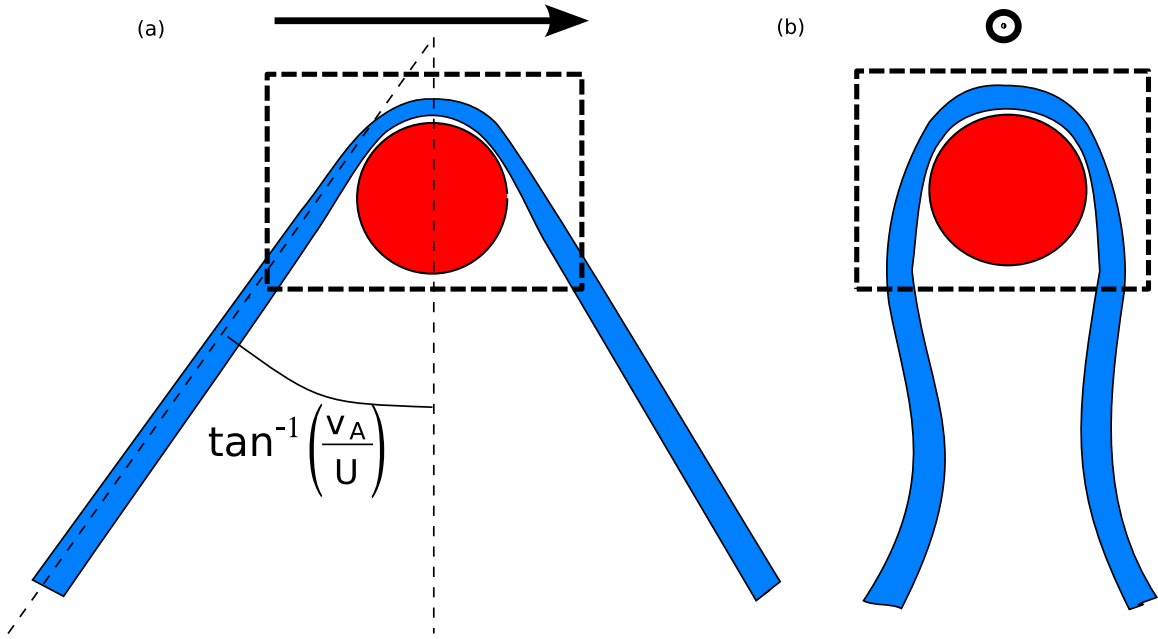
Fig. 4.— A cartoon showing the expected geometry of the draped magnetic field (blue) over the object (red). Seen in the plane of the direction of the ambient field, panel (a), with the direction of the ambient field shown, a clean bow wave is presented with a well-defined opening angle. In the plane perpendicular to the ambient field, panel (b), the field lines can slip around the projectile, and the flow would close back in on a stagnation line on the other side of the object except for largely-2d vortical motions induced by instabilities at the magnetic interface. The geometry of the flow in the region indicated by dashed box depends heavily on the final shape, and thus internal structure, of the moving object.

This buildup of magnetic field will greatly effect the flow in the direction of the ambient field lines, and the projectile will leave a magnetic bow wave behind it; by analogy with other similar bow waves, we expect it to have an opening angle of $\tan\theta \approx v_A/u$. In the plane perpendicular to the ambient magnetic field, however, the magnetic field will have a much less direct effect as field lines can simply slip around the projectile and instabilities can occur. In the potential flow simulation, the flow smoothly reattaches at the rear of the projectile; however, in this case, vortical motions generated at the magnetic contact (where the magnetic pressure and magnetic tension force is misaligned with the density gradient) and by instabilities at the magnetic interface (which are not stabilized in this plane) detach the wake from the object, leaving largely two-dimensional vortical motions along the field lines in this plane. The resulting expected geometry is shown in

Initial magnetic field in the plane:

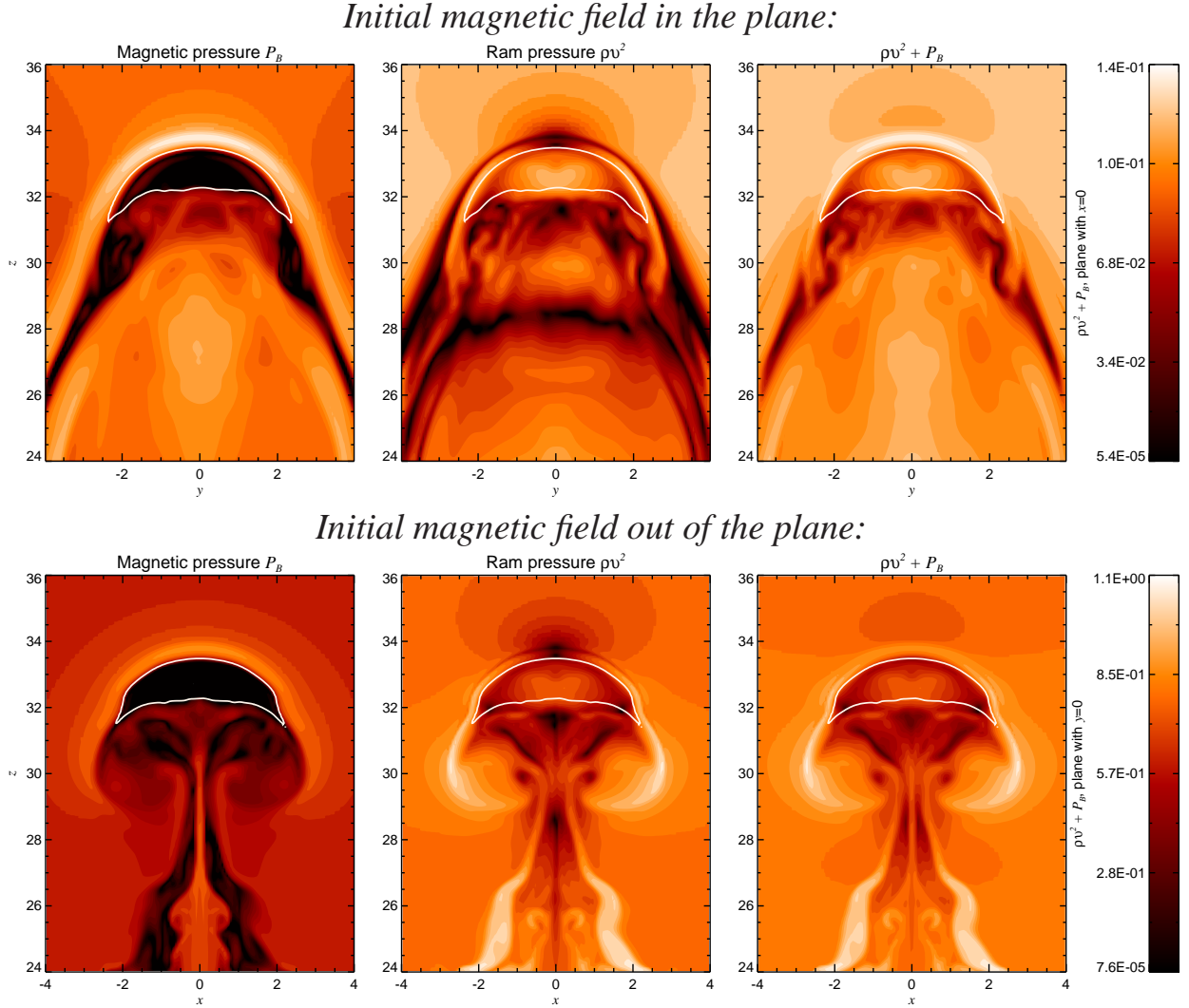

Initial magnetic field out of the plane:

Fig. 5.— We compare the draped magnetic pressure and ram pressure in the plane that is parallel (perpendicular) to the initial magnetic field in the top (bottom) panels with a logarithmic color scale. In the parallel plane, the overpressure of the magnetic draping layer is only partly compensated by a deficit in ram pressure and eventually is responsible for decelerating the core due to magnetic tension. In the perpendicular plane, the ram pressure in the wake of the core attains much higher values and the draping layer closes towards the symmetry axis unlike the parallel plane where a nice opening cone forms. Shown here is a zoom-in on a small region of our computational domain.

a cartoon in Fig. 4 and for our simulation in Fig. 5. This shows that the draping layer becomes dynamically important and fills in the deficit of ram pressure. The sum of the magnetic and ram pressure shows an over-pressure ahead of the core that leads to a deceleration of the projectile.

3. METHODOLOGY

In order to understand the full non-linear physics of magnetic draping around a dynamically evolving dense projectile moving in a magnetized plasma we perform our analysis in two steps. First, we analytically study the properties of the flow of an ideally conducting plasma with a frozen-in magnetic field around a sphere to explore the characteristics of the magnetic field near the surface of the body. To this end, we disregard any possible change in the flow pattern by means of the back-reaction of the magnetic field. While the derivation of this problem can be found in Appendix A, we summarize the key results in this section. In the second step, we compare this analytical solution to an MHD adaptive mesh refinement simulation and explore it quantitatively.

3.1. Analytical solution

The potential flow solution for an incompressible flow around a spherical body reads as

$$v = e_r \left(\frac{R^3}{r^3} - 1 \right) u \cos \theta + e_\theta \left(\frac{R^3}{2r^3} + 1 \right) u \sin \theta, \tag{3}$$

where R denotes the radius of the sphere and u is the speed of the core through the quiescent ambient fluid. Using this solution, we solve for the resulting frozen-in magnetic field while neglecting its back-reaction onto the flow. For convenience, we show here the approximate solution which is valid near the sphere,

$$B_r = \frac{2}{3} B_0 \sqrt{\frac{3s}{R}} \frac{\sin \theta}{1 + \cos \theta} \sin \phi, \tag{4}$$

$$B_\theta = B_0 \sin \phi \sqrt{\frac{R}{3s}}, \tag{5}$$

$$B_\phi = B_0 \cos \phi \sqrt{\frac{R}{3s}}, \tag{6}$$

where we introduced a radial coordinate from the surface of the sphere, namely $s = r - R$. These approximate solutions uniformly describe the field near the sphere with respect to the angle θ. As described in Appendix A, the energy density of the magnetic field forming in the wake behind the body is predicted to diverge logarithmically. We point out that the validity of the potential flow solution heavily relies on the smooth irrotational fluid solution where the magnetic back-reaction is negligible. We will see that these assumptions are naturally violated in the wake.

3.2. Numerical solution

3.2.1. Setup

The simulations presented in this paper are set up as shown in Fig. 6. For clarity of under-standing the physical picture, we consider only the magnetohydrodynamics (MHD); no external- or self-gravity is considered, and we defer other physics such as self-consistent inclusion of ther-mal conductivity to future work. In this report, we also consider only the magnetic field of the external medium, and assume that it is uniform over the scales of interest here.

In the code units we consider here, the ambient material has a density of $\rho_0 = 1$, and a gas pressure $P = 1$. The (unmagnetized) fiducial projectile has a radius that we vary in our runs between $R = 0.5$ and 2, and a maximum density of $\rho_{\text{max}} = 750$. With the density profile chosen $\rho(r) = \rho_{\text{max}}(1 + \cos(\pi r/R))/2$, the mean density of the projectile is $(1 - 6/\pi^2)\rho_{\text{max}}/2 \approx 0.2\rho_{\text{max}}$. Both the ambient and projectile material are treated as ideal, perfectly conducting fluids with ratio of specific heats $\gamma = 5/3$, and so the adiabatic sound speed in the ambient medium is $\sqrt{5/3}$. The pressure inside the projectile is chosen so that the material is initially in pressure equilibrium.

The projectile initial velocity is typically chosen to be $1/4$, for a Mach number into the the ambient medium of ≈ 0.32. The simulation in the transverse directions range from $[-4, 4]$, and in the direction of motion of the projectile ranges from $[0, 28]$ for an aspect ratio of 2:7; in most of the simulations with projectiles larger than the fiducial $R = 1$, the domain size is increased proportionately. The initial magnetic field strength can be defined in terms of $\alpha_0 = \rho u^2/P_{B_0}$; a typical value used in these simulations is $25/4$, or $P_{B_0} = 1/100$. Periodic boundary conditions are used in the directions perpendicular to the direction of motion, and zero-gradient 'outflow' conditions are used in the z direction. Experiments with different horizontal boundary conditions produced no major differences in results.

The projectile fluid is initially tagged with a passive scalar, so that the material corresponding to the projectile can be traced throughout the simulation.

3.2.2. Code Choice

As can be seen from analytic arguments, and is shown in some detail in §2, two features char-acterize the problem of magnetic draping: the formation of a narrow strongly-magnetized layer, and the relative simplicity of the dynamics, in that a potential flow solution with only magnetic field kinematics captures much of the problem, lacking only the magnetic field back-reaction.

Because of the separation of scales (a relatively large object moving through an ambient
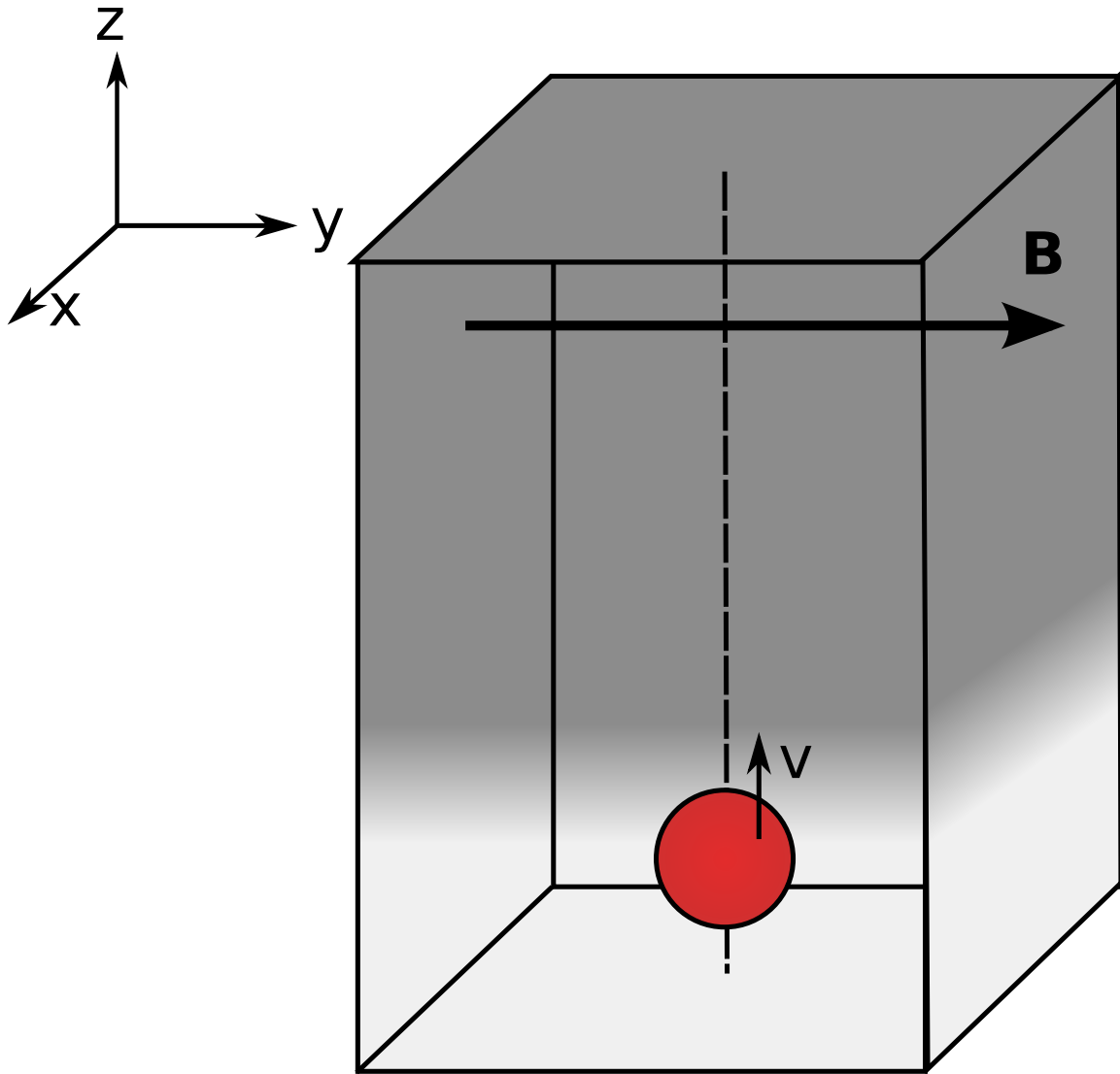
Fig. 6.— Diagram showing the geometry of the simulations presented here. A spherical projectile with a smooth density profile $\rho_{max}(1 + \cos(\pi r/R))/2$ is sent in the $+z$ direction with an initial velocity v through an ambient medium with density ρ_0 and a uniform magnetic field pointed in the $+y$ direction. The magnetic field strength 'turns on' through the domain with a tanh-profile in the direction of motion of the projectile, as indicated by the shading of the box; this allows us to start the core in an essentially field-free region and smoothly enter the magnetized region. Periodic boundary conditions are used in the directions perpendicular to the direction of motion, and zero-gradient 'outflow' conditions are used in the z direction.

medium and a relatively small layer forming around it), the highest resolution requirements would impose a large cost on the simulations if the resolution had to be everywhere uniform; indeed, it is only a small portion of the simulation domain which needs to be resolved at the highest level. This is especially true since the simulations we will need to perform are three-dimensional (as we will see in the next sub-section, it is impossible to do meaningful simulations of magnetic draping in two dimensions). Thus, a simulation code which allows some adaptivity of meshing is extremely helpful for approaching this problem.

The relatively straightforward magnetic field dynamics means that, unlike in problems of (for instance) studying the details of MHD turbulence, we do not require high-order finite difference methods; this is particularly true because of the sharpness of the thin layers and the large density gradients in this problem. Instead, an MHD solver which can accurately deal with sharp gradients is valued.

As a result of the importance of AMR for these simulations, the code we've chosen to perform these simulations with is the FLASH code (Fryxell et al. 2000; Calder et al. 2002). FLASH is an adaptive-mesh general purpose astrophysical hydrodynamics code which is publicly available[1]. The MHD solver we use here is a dimensionally-split second-order accurate 8-wave Godunov-type solver which is described in more detail in Powell et al. (1999). The smallness of spurious magnetic monopoles is ensured by a diffusion-type 'div-B' clean operation. This diffusive cleaning approach can be problematic near strong shocks, where diffusion cannot operate quickly enough; however, no such shocks occur in these simulations. FLASH has been often used for related problems such as hot and magnetized bubbles in the intercluster medium (*e.g.*, Robinson et al. 2004; Pavlovski et al. 2007; Heinz et al. 2006; Roediger et al. 2006; Gardini 2006; Pope et al. 2005; Dalla Vecchia et al. 2004; Heinz et al. 2003; Brüggen 2003; Brüggen and Kaiser 2002).

3.2.3. *Parameters*

Performing simulations of draping over a projectile with an explicit hydrodynamics code (so that compressibility effects will be included, for ease of comparison with later, supersonic, work) with a finite resolution places some restrictions on the range of parameter space which can be explored.

For simulating these cases with no leading shock, we require that the velocity of the projectile, u, be less than the sound speed in the ambient fluid – but to take a reasonable number

---

[1]http://flash.uchicago.edu

of timesteps (avoiding computational expense and spurious diffusion) requires that the projectile velocity remain of the order of the sound speed; thus $u \lesssim c_s$, or $\rho_0 u^2 \lesssim \gamma P$, where ρ_0 and P are the unperturbed density and pressure of the ambient medium. For the hydrodynamics of draping to be realistic, the magnetic pressure in the fluid must be significantly less than the gas pressure, $P_{B_0} \ll P$. Finally, resolution requirements for resolving the thickness of the magnetic layer will put some constraint on the thickness of the magnetic layer $l > R/N$ from Eq. 2, with N being the number of points which resolve the radius of the projectile; typically the size of the domain (if at full resolution) will be $8N \times 8N \times 28N$. This constraint, expressed in terms of the relevant pressures (ram pressure and initial magnetic pressure) $P_{B_0} \gtrsim 3\alpha(\rho_0 u^2)/N$. Combined, these constraints give

$$\gamma P \gtrsim \rho_0 u^2 \gg P_{B_0} \gtrsim \frac{3\alpha\rho_0 u^2}{N} \tag{7}$$

For a given u – which is more or less arbitrary, fixed to be near the (arbitrary) sound speed – there is thus a relatively narrow range of initial magnetic pressures in terms of the ram pressure of the ambient material onto the projectile which can be efficiently simulated. As we will see, $\alpha \approx 2$, and for the simulations presented here, $N \sim 32 - 64$, meaning we are constrained to study roughly that part of parameter space where $\rho_0 u^2/P_{B_0} \approx 1 - 10$.

3.2.4. *Two Dimensional Results*

In two dimensions, the imposition of a symmetry greatly limits possible magnetic field geometries. In an axisymmetric geometry, the only meaningful uniform field geometry is parallel to the axis of symmetry, which in this case would also be the direction of motion of the projectile; in this somewhat artificial case magnetic field could somewhat constrain a projectile (or a bubble; Robinson et al. (2004)) but draping could not occur.

In planar symmetry, the field can have components out of the plane, in the plane parallel to the direction of motion, or in the plane perpendicular to the direction of motion. A component out of the plane will only have the dynamical effect of adding to an effective gas pressure ((*e.g.*, Chandrasekhar 1981)); the component along the direction of motion of the projectile cannot be draped.

Previous work (*e.g.*, Asai et al. 2005) has examined the case with two dimensional planar symmetry with a magnetic field in the plane of the simulation and perpendicular to the direction of motion of the projectile. However, in this case, field lines cannot cannot slip around the projectile, and so as more and more magnetic field gets swept up by the projectile, magnetic tension grows monotonically and linearly ahead of the projectile until the forces becomes comparable not only to the ram pressure seen by the projectile of the ambient medium, but to the ram pressure of the

projectile as seen by the ambient medium. At this point, the projectile trajectory is reversed. A figure describing this is shown in Fig. 7, where the magnetic tension forces are seen to compress the projectile (with mean density ≈ 150 times that of the magnetized medium) before repelling it.

This outcome is hinted at in Fig. 4 of Asai et al. (2005), where in 2d the magnetic energy increases linearly and without bound, while the 3d models reach a maximum magnetic energy.

3.2.5. *Three Dimensional Simulations*

A listing of the eight main runs done for this work are shown in Table 3.2.5, and the basic setup follows the discussion earlier. The parameters varied are the size of the projectile, its velocity, and the strength of the ambient magnetic field. Other runs (the equivalent of run B but with half the resolution, or with the same resolution but differing boundary conditions) were run to confirm that the results did not change; they are not listed here.

Run	R	u	$P_{b,0}$	$\rho u^2 / P_{b,0}$	$R/\Delta x$
A	$\frac{1}{2}$	$\frac{1}{4}$	$\frac{1}{100}$	6.25	64
B	1	$\frac{1}{4}$	$\frac{1}{100}$	6.25	64
C	2	$\frac{1}{4}$	$\frac{1}{100}$	6.25	32
D	1	$\frac{1}{4}$	$\frac{1}{50}$	3.125	64
E	$\frac{1}{2}$	$\frac{1}{8}$	$\frac{1}{100}$	1.5625	32
F	$\frac{1}{2}$	$\frac{1}{4}$	$\frac{1}{100}$	6.25	32
G	$\frac{1}{2}$	$\frac{1}{2}$	$\frac{1}{100}$	25	32
H	2	$\frac{1}{4}$	$\frac{1}{250}$	15.625	128

Table 1: Details of 3-dimensional simulations run for this work. Simulations were run with an ambient density and pressure of 1 in code units, and $\gamma = 5/3$. Simulations were run until maximum magnetic field on stagnation line was approximately constant, typically 40-80 time units.

To show that these runs were producing results independent of resolution, the maximum magnetic field strength along the stagnation line for all the runs with the same P_{B0} and ρu_0^2 are plotted versus time in Fig. 8. The maximum field strength is sensitive to the resolution of the magnetic field layer, but we see here that varying the resolution by a factor of two does not effect the results, as the field layer is adequately resolved (but only marginally in the case of $R/\Delta x = 32$). We also see, as we'd expect from the discussions in §2, that the field strength in the layer does not depend on the size of the core.

The magnetic layer in Run G is under-resolved; while the value of $R/\Delta x$ is the same as other runs, the velocity is higher, so that by Eq. 2 the layer is thinner. We include this run because it
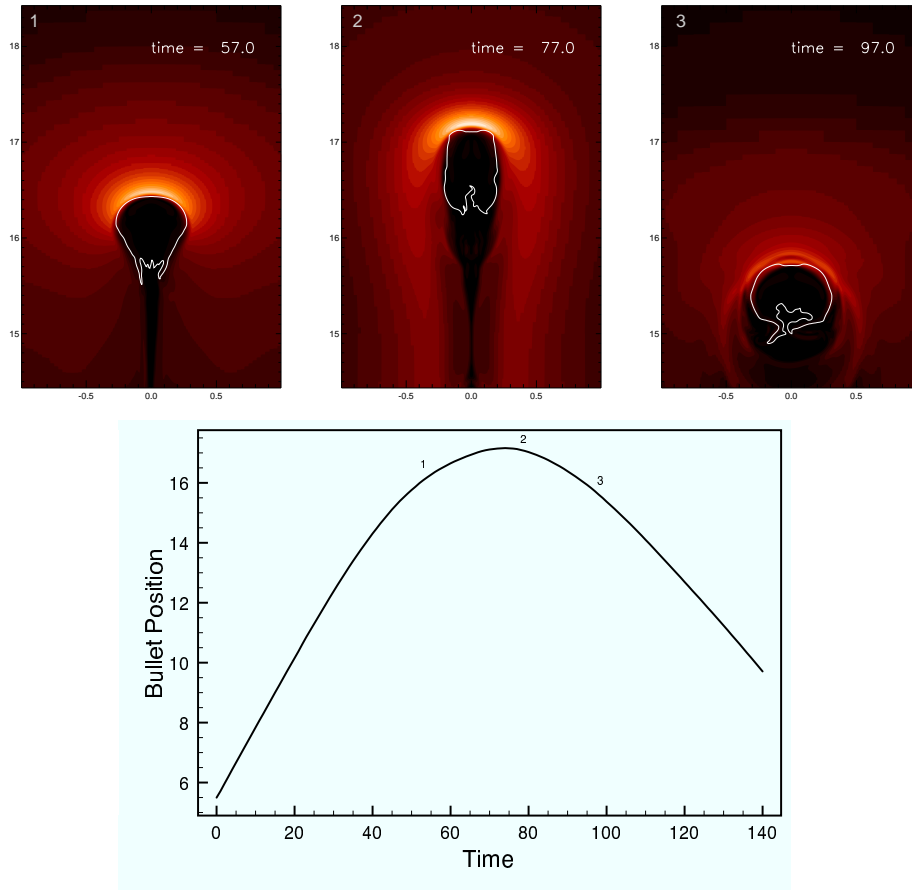
Fig. 7.— The above is a plot of the projectile position (calculated here by the maximum height at which there is significant projectile material at any given time) over time in a two dimensional draping simulation. At about time 75, the projectile is actually bounced back under the extremely strong magnetic tension which in two dimensions must grow ahead of the projectile. The top panel shows B^2 in a closeup of the simulation domain at three representative times during the bounce, with a white contour indicating the position of the original projectile material.
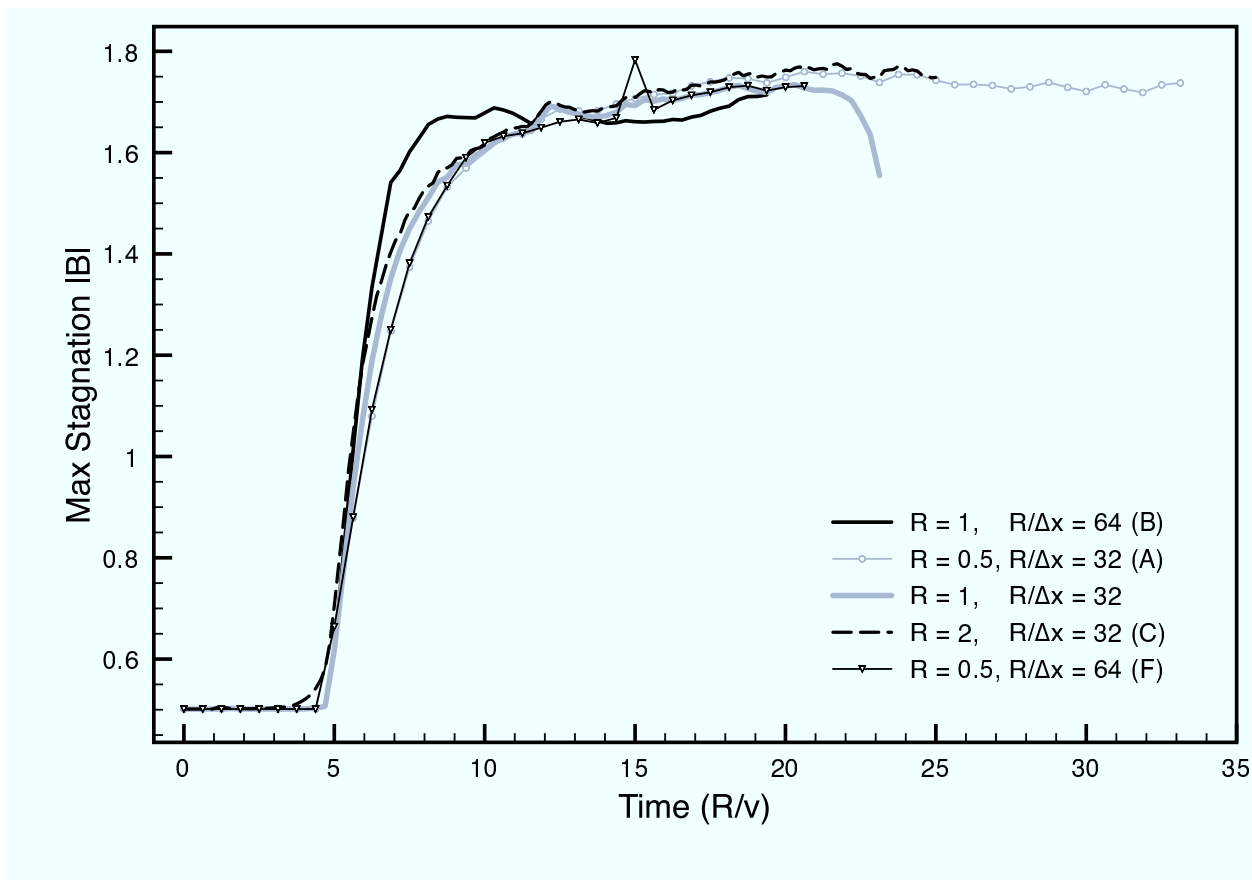
Fig. 8.— A plot of the maximum magnetic field strength along the stagnation line for runs with three different projectile sizes and two different resolutions across the projectile, all with the same velocity into the ambient medium and the same ambient magnetic field. Plotted is the maximum magnitude of the magnetic field along the stagnation line vs the time (scaled to the crossing time of the projectile). The projectile initially sits in an unmagnetized region. The maximum magnetic field strength along the stagnation line is a sensitive measure of whether the structure of the draped magnetic field is being resolved; we see here clear evidence that with the resolution used in this simulation the draped layer is being adequately resolved. In the low-resolution $R = 1$ simulation, which also was run in a somewhat smaller box, towards the end of the run the draping layer begins to leave the top of the simulation domain, leading to the sudden rapid drop in magnetic field strength.

demonstrates certain robustness of results; although the layer structure is not adequately resolved at the stagnation point, other global properties of the magnetic layer (geometry and dynamical effects) otherwise remain robust.

Indeed, one should be careful about what one means by 'resolved'. This discussion should not be taken to mean that the other simulations are in all respects resolved. In particular, as we will see in §4 and §5, and as suggested by Dursi (2007), the flow around the bubble in the xz plane (*e.g.*, transverse to the initial magnetic field) is unstable to Kelvin-Helmholtz and Rayleigh-Taylor instabilities, not stabilized by the presence of magnetic field. Since we have not prescribed any small-scale dissipative physics in these simulations, these instabilities will never properly converge with increased resolution (*e.g.*, Calder et al. 2002) as new unstable scales are added. This can only be corrected by adding small-scale physics, *e.g.* thermal diffusion; this is left for future work, as the relevant microphysics is itself a current research problem Lyutikov (2007); Schekochihin et al. (2007). While the rate of development of the instabilities and their properties is very important for long-term mixing of the material of the moving object with that of the surrounding medium, we restrict ourselves here to studying the development of the magnetic layer and its global properties.

Another thing worth noting in our runs is that for run E, $\mathcal{M}_A^2 = 1/2(\rho u^2/P_{B0}) \approx 0.78 < 1$; that is, this run has the projectile moving sub-Alfvénically, if only marginally. However, because of the field geometry, we will see that this makes essentially no difference for the draping. This is simply because the Alfvén speed in the direction of motion of the projectile is zero – no component of the magnetic field points in that direction. While the exact imposition of this condition in our initial conditions is somewhat artificial in this case, it is always true that it is only the component of the magnetic field that lies transverse to the direction of motion that will be draped.

4. COMPARISON OF THEORY AND SIMULATIONS

4.1. Magnetic field along the stagnation line

The first comparison we make is to the one-dimensional predictions made along the stagnation line, for instance in Lyutikov (2006), where a very specific prediction is made for the ramp up, with a particular functional form, of the magnetic field strength given in Eq. 1, and it is not necessarily clear that such a prediction will hold when the projectile begins to deviate significantly from spherical.

To make this comparison, we extract the magnetic field strength along the stagnation line for

an output, and fit it to the equation

$$\frac{|B|}{\rho} = \frac{B_0}{\rho_0} \frac{1}{\sqrt{1 - \left(\frac{R}{(z-z_0)}\right)^3}} \tag{8}$$

where B_0, ρ_0 are known, and the fit is for the parameters R, which would correspond to the radius of the sphere, and z_0, which would be the position of the centre of the sphere. Results for a typical output are shown in Fig. 9. Not only do the fits well represent the behaviour magnetic field strength, but they also suggest a physical interpretation for the functional forms interpretation even when the projectile becomes significantly non-spherical; R becomes the radius of curvature of the working surface of the projectile at the stagnation line. As the projectile becomes more distorted, R can become significantly larger than the initial radius of the projectile; in this example, the expansion is a relatively modest 15%.
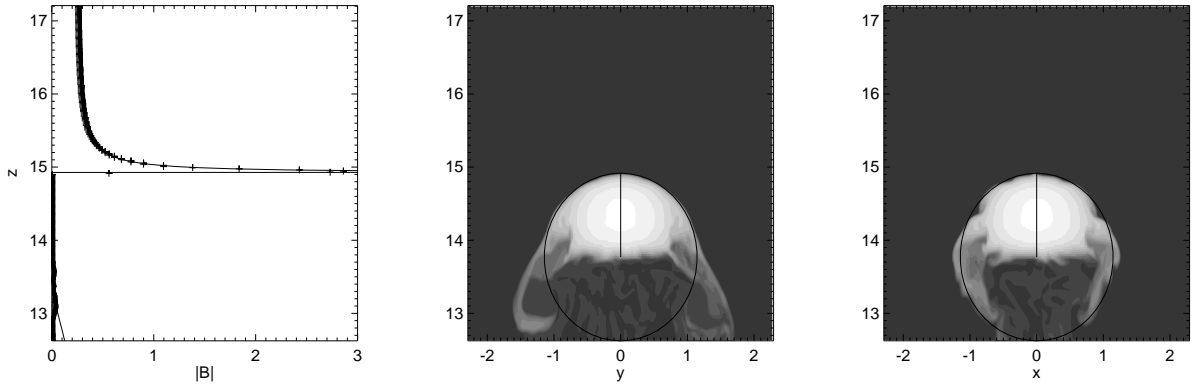

Fig. 9.— Shown is, left, the magnetic field along the stagnation line in the simulation ('+') and a fitted theory prediction, with the two fitting parameters being the position of the peak and a radius giving a characteristic fall off of the field strength. On the right are cut-planes along and across the initial magnetic field of the density of the projectile, with a circle of radius and position given by the fit to the magnetic field structure, left. The radius given by the fit corresponds with the radius of curvature at the working surface of the projectile. Results are taken from run B at time $t = 38.75$; results from other simulations and other times give similarly good fits.

4.2. Comparison of the velocity field

To compare the potential flow calculations, done in the frame of the spherical body, with those of the numerical simulations, we transform the numerical simulations into the frame of the projectile. Because the projectile slows down over time, we do not use the initial velocity u_0 for
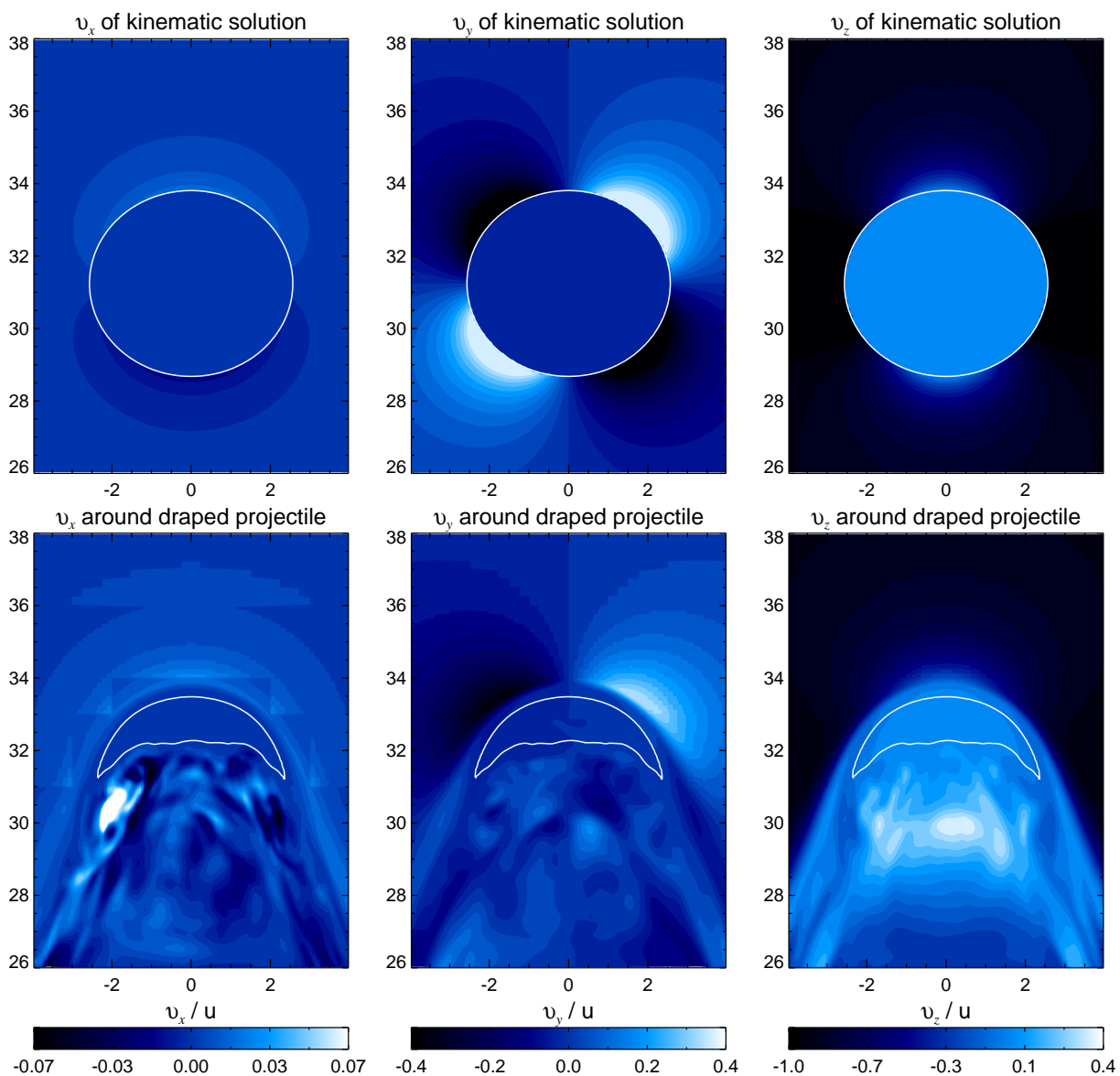
– 19 –

Fig. 10.— Comparison of the velocity field of the analytical solution in the kinematic approxima-
tion (top panels) with our numerical simulation (bottom panels) in the plane of the initial magnetic
field. While the velocity fields resemble each other very well in the upper half-space, there are
distinct differences in the lower half-space. These are due to the non-linear back-reaction of the
dynamically important magnetic field in the draping layer on the MHD flow that generates vorticity
in the wake of the projectile (cf. §5.4). Shown here and in the next figures is a zoom-in on a small
region of our computational domain that extends up to 112 length units and is four times larger in
x and y direction. Note that we symmetrized the color map of the v_x-component in order not to be
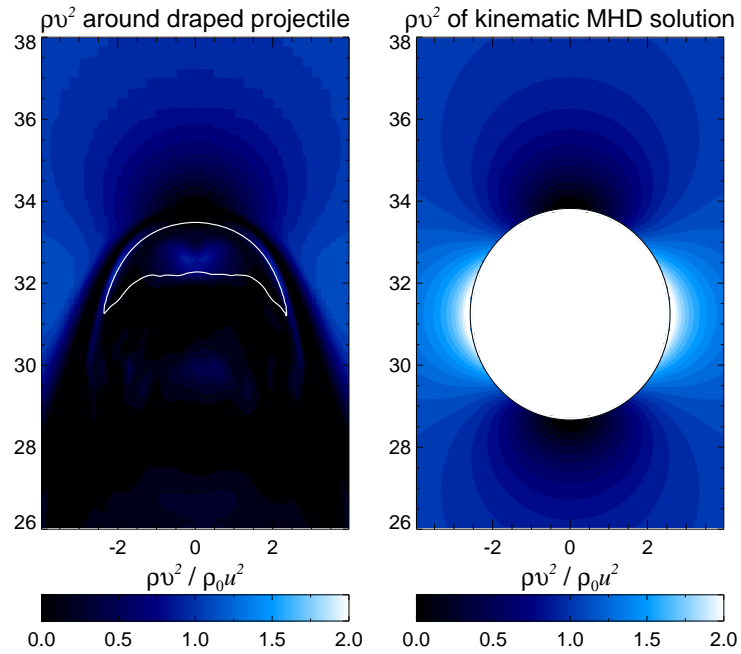dominated by one slightly larger eddy.

Fig. 11.— Comparison of the ram pressure in our numerical simulation (left panel) with the analytical solution in the kinematic approximation (right panel). Ahead of the projectile, the ram pressure resembles an exact potential flow behavior up to the draping layer which can be seen as a black layer around the projectile with a deficit of hydrodynamical pressure. Non-linear magnetic back-reaction of the draping layer causes the flow to depart from the potential flow solution and to develop vorticity.

this transformation, but measure the instantaneous mass-weighted velocity of the projectile, by making use of the fact that we are tracking the fluid that initially resided in the projectile by use of an advected passive scalar, a. Thus we measure the instantaneous velocity of the projectile as

$$u = \frac{\langle \rho a v_z \rangle}{\langle \rho a \rangle}. \tag{9}$$

The top panels of Fig. 10 show the analytical solution of the velocity field around the spherical body with radius R in the kinematic approximation. For convenience and to simplify the comparison to the magnetic field visualization, we show the Cartesian components of the velocity field. At infinity, the fluid is characterized by a uniform velocity $v = -e_z u$. The quadrupolar flow structure results from the fluid decelerating towards the stagnation line, the successive acceleration around the sphere until $\theta = \pi/2$ and mirroring this behavior in the lower half-plane by symmetry. The bottom panels of Fig. 10 show the numerical solution of the velocity field around an initially spherical projectile that deformed in response to the non-linear evolution of the magnetized plasma. The white line reflects the 0.9 contour of the 'projectile fluid' and corresponds to an iso-density contour.[2] The quadrupolar flow structure in the upper half-plane resembles nicely the analytic potential flow solution. As the flow approaches the projectile and surrounds it, there are important differences visible. In the analytical solution, the flow accelerates for $\theta \le \pi/2$ and decelerates for larger angles θ. In the numerical solution, the magnetic draping layer is stationary with respect to the projectile. This causes the flow almost comes to rest in the magnetic draping layer. The back-reaction of the magnetic draping layer on the flow casts a 'shadow' on the wake of the projectile. It prevents the flow to converge towards the symmetry axis and suppresses the deceleration of the flow. Instead, vorticity is generated at the draping layer which will be studied in detail in §5.4. The comparison of the ram pressure in Fig. 11 underpins this argument.

4.3.   Comparison of the magnetic field

It is instructive to compare the analytic solution of the frozen-in magnetic field in the kinematic approximation to the numerical solution in the planes that are parallel and perpendicular to the initial magnetic field. We compare the individual Cartesian components of the field (Fig. 12 and 13) as well as the magnetic energy density in Fig. 14. Note that we only show a Taylor expansion of the highly complex exact solution as derived in Appendix A. Strictly, this solution applies only near the sphere with an accuracy to $O((r - R)^{3/2})$ as well as for flow lines that have small

---

[2]Note that the apparent grid structure seen in the upper part of our simulated v_x-component is an artifact of our plotting routine as well as small grid noise. The interpolation scheme of the plotting routine falsely interpolates a smooth velocity gradient with an entire AMR block while it actually drops quickly to the velocity value at infinity.
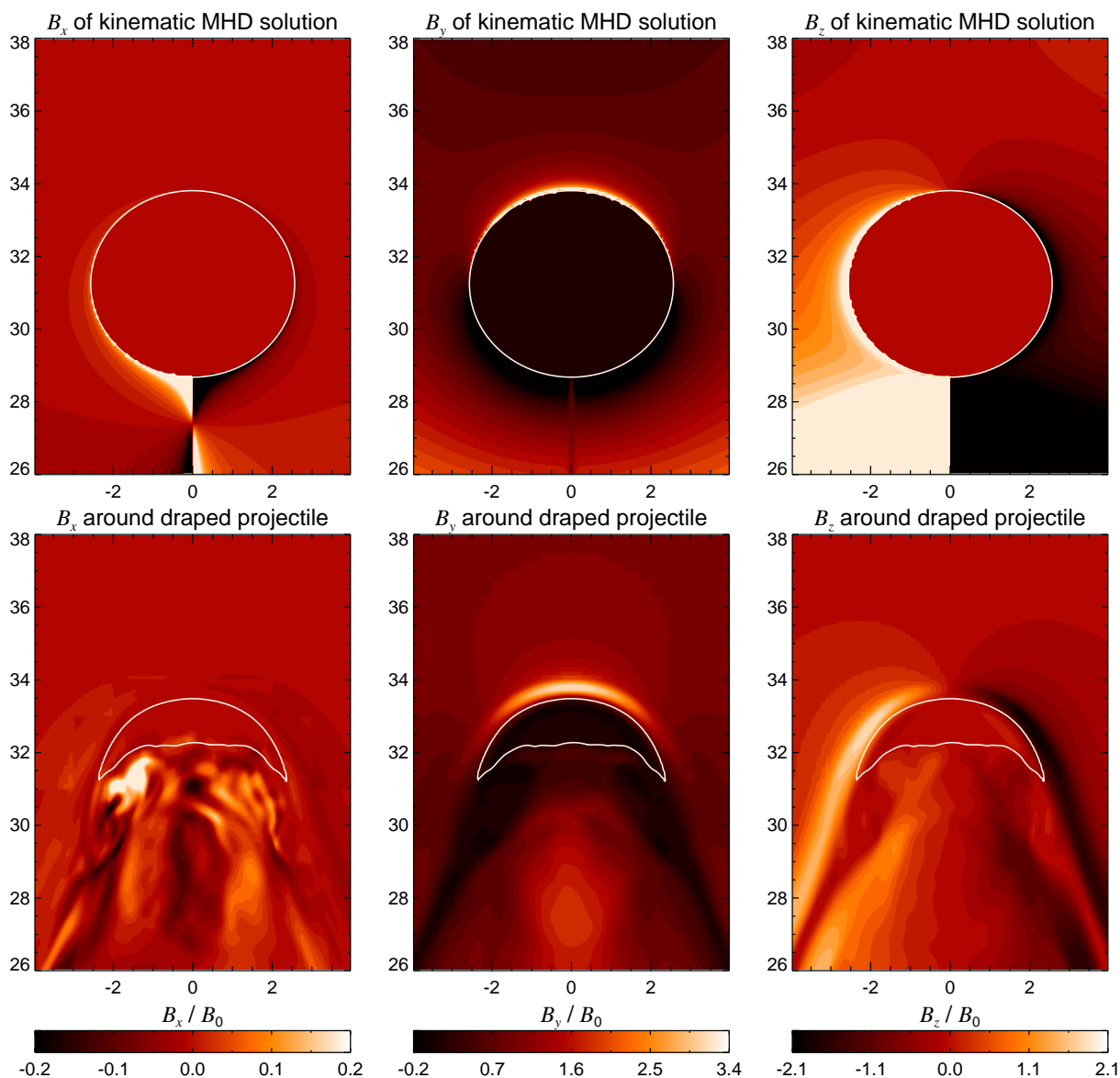
Fig. 12.— Comparison of the magnetic field in our numerical simulation (bottom panels) with the Taylor expansion of the analytical solution in the kinematic approximation that strictly applies only near the sphere (top panels). We show the Cartesian components (left to right, x, y, z) of the magnetic field in the plane that is parallel to the initial magnetic field. There is a nice agreement between both solutions in the upper half-space, while there are again distinct differences in the lower half-space. The magnetic shoulders behind the projectile can be identified that prevents the draping layer from contracting towards the symmetry axis. In addition, MHD turbulence starts to develop in the wake of the projectile.
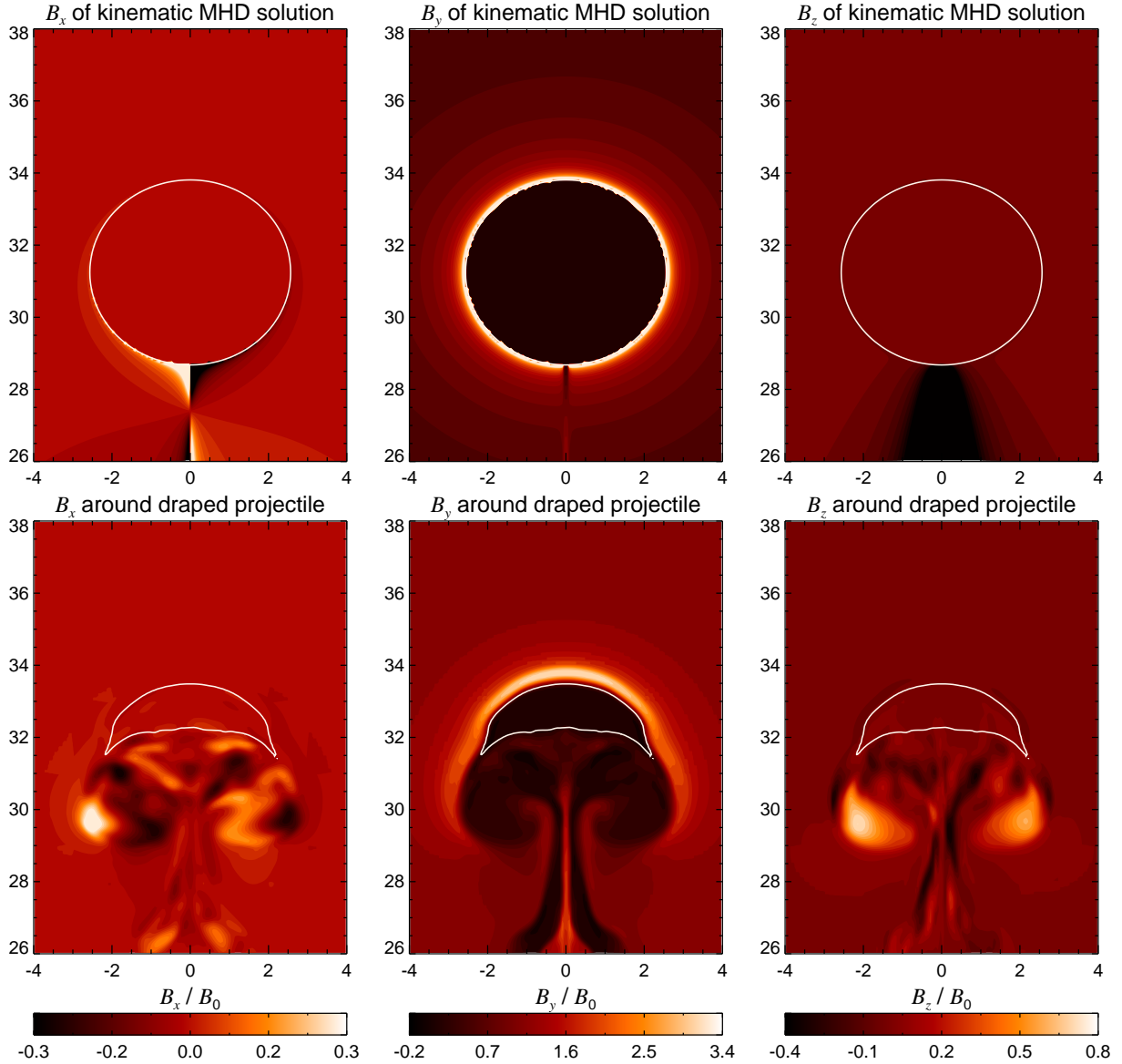
Fig. 13.— Same as previous figure, but in the the plane that is perpendicular to the initial magnetic field. Shown is, left to right, the x, y, z components. As expected from our analytic solutions, the draping layer forms by piling up magnetic field lines ahead of the projectile. The irregular magnetic field in the wake is generated by the vorticity that is absent by definition in our potential flow solution.

Initial magnetic field in the plane:

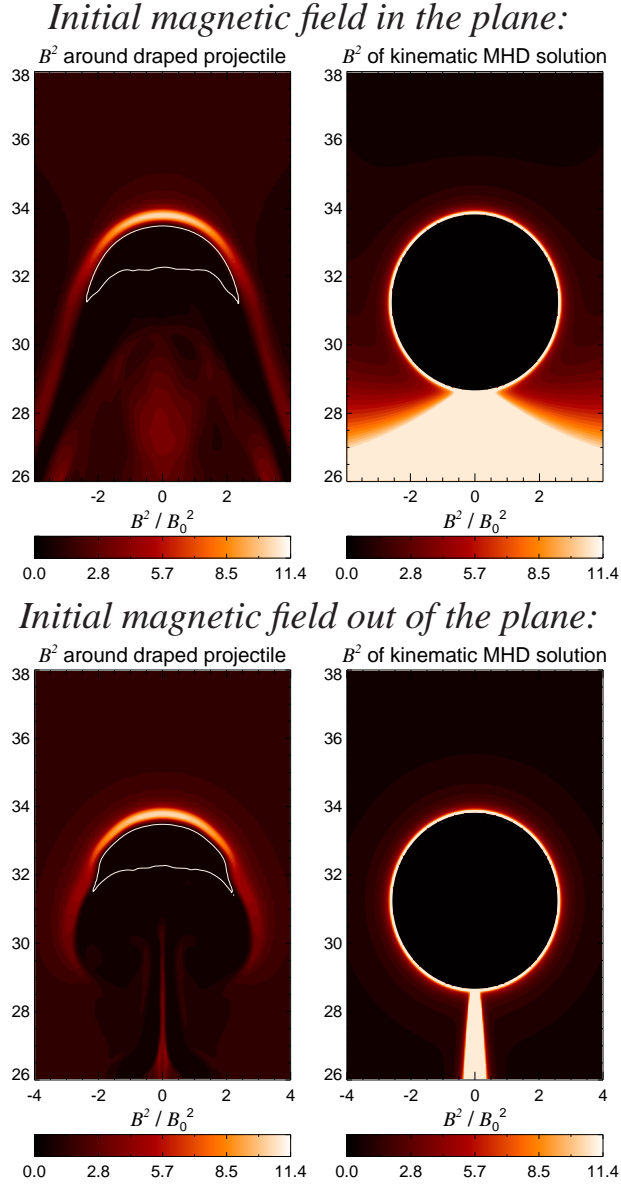*Initial magnetic field out of the plane:*

Fig. 14.— Comparison of the magnetic energy density in our numerical simulation (left panel) with the analytical solution in the kinematic approximation (right panel). The top (bottom) panels show the plane that is parallel (perpendicular) to the initial magnetic field. In the analytical solution there is a narrow magnetic layer draped around the spherical body, while in our simulations the draping layer peels off behind the projectile due to vorticity generation. The geometry of the magnetic draping layer in the upper half-plane is very similar in both planes suggesting there an approximately spherical symmetry. In the wake of the projectile, the draping layer forms a characteristic opening angle while the field lines can swipe around the projectile in the perpendicular plane and the draping layer closes towards the symmetry axis.

impact parameters initially at infinity. Using a different expansion, we verified that the general solution has the appropriate behavior of the homogeneous magnetic field at infinity in the upper half-space pointing towards the positive y-coordinate axis, i.e. rightwards in Fig. 12. As expected, the y-component of the magnetic field increases as we approach the sphere since the field lines are moving closer to each other. In the immediate vicinity of the sphere, the B field attains a dipolar z-component as the field lines are carried around the sphere with the fluid and causes them to bend in reaction to the ram pressure of the sphere. As pointed out by Bernikov and Semenov (1980) the magnetic lines of force that end at the stagnation point are strongly elongated as the swipe around the sphere parallel to the line of flow reaching from the stagnation point into the rear. This leads to the unphysical increase of the magnetic field as it approaches the line of symmetry in the wake and eventually to a logarithmic divergence of the magnetic energy density there.

In the upper half-plane, the analytic solution matches the numerical one closely. Interestingly, in the region behind the deformed projectile, a *magnetic draping cone* develops that stems from the dynamically important draping layer that has swiped around the sphere and advected downstream the projectile. In addition, the magnetic pressure in the wake of the projectile is also amplified by a moderate factor of roughly five (cf. Fig. 14). We will show further down, that this field is generated together with vorticity in the draping layer. In the *parallel plane* to the initial magnetic field, the magnetic draping cone causes the stationary flow not to converge towards the symmetry axis and protects the region in the wake against the increase of the magnetic energy without bounds. The numerical solution can qualitatively be obtained by remapping the analytic solution for $\theta > \pi/2$ onto the coordinate along the magnetic draping cone. In the *perpendicular plane* to the initial magnetic field, there is even better agreement between the analytic and the numerical solution. The magnetic field in that plane lies primarily in its initial y-direction. This behaviour can easily be understood in terms of the field lines sweeping around the sphere in a laminar flow. Numerically, we simulate the response of the geometry of the projectile to the hydrodynamics. Vortices in the wake deform the projectile leading to a cap-geometry and a mushroom shape of the y-component of the magnetic field. This implies that the flow lines detach from the dense material of the projectile generating furthermore vorticity and MHD turbulence in the wake. The turbulent field mixes the Cartesian components which can be nicely seen in the Fig. 13. The magnetic pressure summarizes our results nicely showing the draping cone in the parallel plane and the mushroom shaped magnetic energy density in the plane perpendicular to that (cf. Fig. 11). Note that we choose the same color scale as derived from the simulations which leads to a saturation of the magnetic energy density in the kinematic approximation at the contact of the spherical body and on the axis in the wake.

5.   CHARACTERISTICS OF MAGNETIC DRAPING

5.1.   Field strength in draping layer

The kinematic solution predicts the magnetic pressure diverges at the stagnation point, which is clearly unphysical. From our discussions in §2 and §4, we expect that the magnetic pressure in the draping layer should be on order ρu^2, at which point the magnetic back-reaction begins to strongly effect the flow; to first order there is no dependence on other parameters, such as background magnetic field. One would expect, too, from looking at figures such as Fig. 5 that the maximum magnetic pressure should exceed the ram pressure by some factor, as the magnetic pressure distribution at the head of the drape is responsible for redirecting the flow in the plane of the draping.

We can test this by plotting, for all our runs, the steady maximum magnetic pressure at the stagnation line (the field quantity that is easiest to consistently characterize) versus the mean ram pressure seen by the projectile, $\rho \langle u \rangle^2$, where $\langle u \rangle$ is the mean of the projectile velocity (calculated as in by Eqn. 9) during the run, and ρ is the ambient density. The plot is shown in Fig. 15 and verifies our expectation.

5.2.   Opening Angle

The magnetic bow wave behind the projectile is expected to propagate transversely away from the projectile at v_A along the field lines, and of course to fall behind the projectile at velocity u. This suggests a natural opening angle in the plane along the magnetic field, $\tan \theta = v_A/u$. That the direction of the scaling is correct can be determined by qualitative inspection of a sequence of 3d renderings of simulation outputs as the velocity changes; e.g., Figs. 16,1,18 for $u = 1/8, 1/4, 1/2$ and v_A fixed at 0.1414.

Although the field lines are stretched during the draping, it is the initial v_A that is relevant, as the stretching of the field lines in the z-direction do not effect the propagation speed in the y-direction. For instance, consider a $\hat{\mathbf{z}}$-velocity shear in y, $v = (0, 0, y/\tau)$, with $\mathbf{B} = (0, B_0, 0)$. The induction equation gives us $\dot{\mathbf{B}} = \nabla \times (v \times \mathbf{B}) = (0, 0, B_0/\tau)$, so that the magnetic field is only changed in the $\hat{\mathbf{z}}$-direction; thus $v_{Ay} = v_A \cdot \hat{y} = v_A \hat{\mathbf{B}} \cdot \hat{y} = (|B|/\sqrt{4\pi\rho})(\mathbf{B} \cdot \hat{y})/|B| = B_y/\sqrt{4\pi\rho} = v_{A,0}$

One can quantify the agreement with this scaling by measuring the opening angle for the drapes in our simulations. The maxima of magnetic field on either side of the stagnation line in the $y - z$ plane are found and tabulated along the z direction of the simulations, and – omitting the regions above or near the projectile itself, and the region below which the drape becomes weaker than transient features in the wake – lines are fit, and the slope gives the (half-)opening angle.
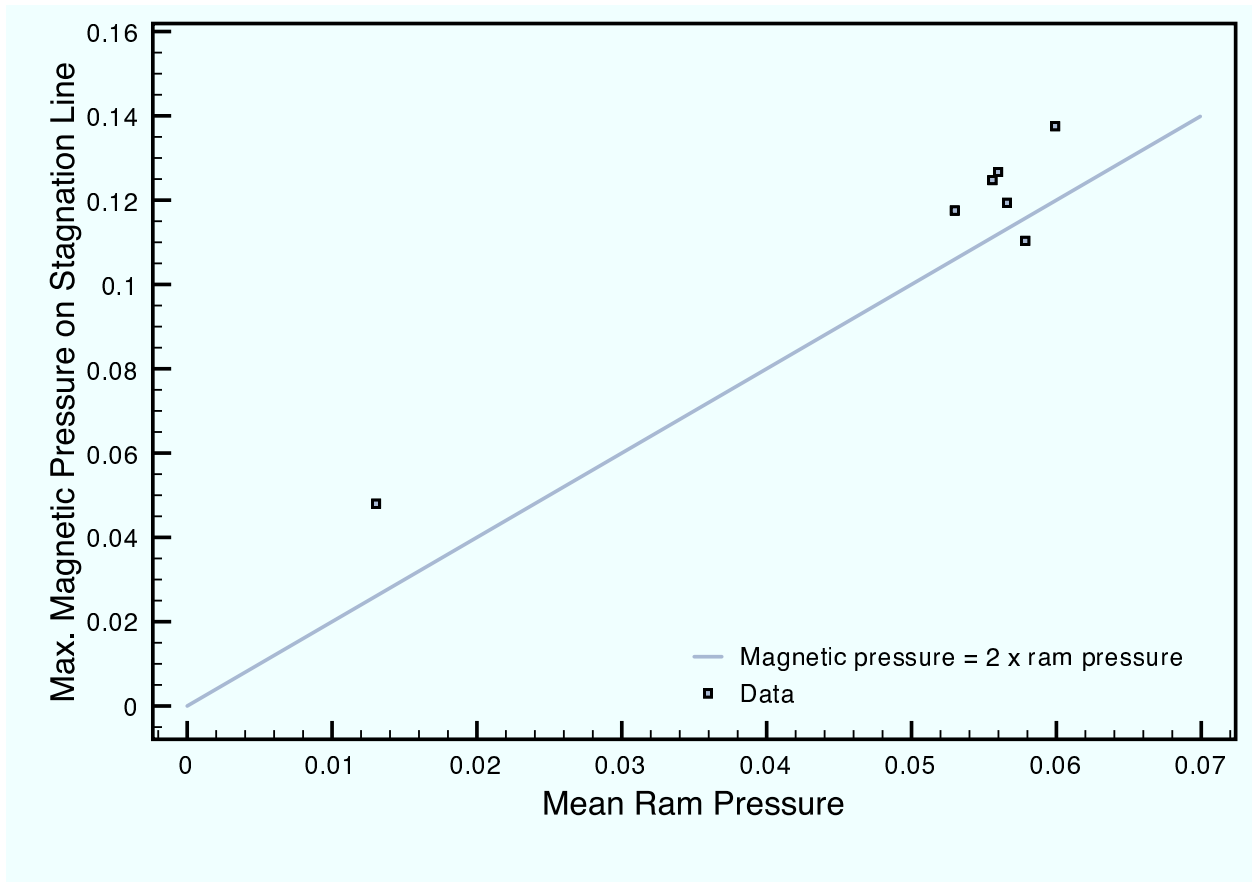
Fig. 15.— A plot for the 3d runs presented here showing the magnetic pressure on the stagnation line once a steady value had been achieved for this quantity as a function of the mean ram pressure $(\rho\langle u\rangle^2)$ as seen by the projectile. Omitted is run G, for which the magnetic layer was under-resolved and thus the maximum magnetic field strength in the layer falls much lower; however, as we will see, even this under-resolution does not strongly effect other global properties of the magnetic drape.

The results of the fitting procedure are shown for the same three simulations in Fig. 20, and a scatter plot for all are runs are given in Fig. 21. The scatter for this quantity, and agreement with the prediction, is somewhat worse than for the other quantities we consider, possibly because the large-scale geometry of the draping is more sensitive to the boundaries and the finite size of the domain than other, more local, quantities.

5.3. Deceleration by magnetic tension

In the scatter plots presented above, we use the mean velocity $\langle u \rangle$ of the projectile over time, because there is a measurable deceleration of the projectile. An example, for run F, is shown in Fig. 22. Before the projectile encounters the magnetic field at $z = 10$, hydrodynamic drag – in principle either (numerical) viscous drag or the the drag force caused by the creation of a turbulent wake – is all that can play a role, and for the simulations presented here, it is the second which dominates. The well-known form for the drag on a sphere is $F_D = 1/2\rho u^2 A C_D$, or in terms of a deceleration,

$$\dot{u}_D = -\frac{3}{8}\frac{\rho u^2}{\langle \rho_p \rangle R}C_D \tag{10}$$

where C_D is the drag coefficient, experimentally known to be between $0.07 - 0.5$, with 0.5 for a turbulent wake, ρ_p is the density and A is the cross-sectional area of the projectile in the direction of motion.

However, once the magnetized region is reached and a magnetic layer built up, then another force acts on the projectile – the magnetic tension from the stretched field-lines. This transition can be seen in Fig. 22 for run F; other runs behave similarly. We see that the deceleration caused by the magnetic field draping is actually significantly stronger than the hydrodynamic draping. This magnetic tension force is $F_T = B^2/(4\pi R)$; we know the magnetic strength in the draping layer scales as ρu^2 (§5.1) and so we can write the deceleration as

$$\dot{u}_T = -\frac{3}{8}\frac{\rho u^2}{\langle \rho_p \rangle R}C_G \tag{11}$$

where C_G is a geometric term taking into account the fact that both the magnetic field strength and radius of curvature of the field lines vary over the 'cap' of the projectile, and we have chosen to normalize C_G so that Eqns. 10 and 11 have the same numeric prefactor for convenience in comparison. We can test this scaling, and at the same time empirically obtain C_G, by plotting the decelerations for our different runs, as is done in Fig. 23; we find $C_G \approx 1.87$.

It is interesting to note first that the two deceleration terms scale in the same way, so that their relative importance remains constant; and that said ordering is such that the magnetic tension

deceleration is always more important, by a factor of ≈ 3.7, for the case of highly turbulent (Re $\approx$ 1000) hydrodynamic drag of $C_D = 0.5$. In the case of our simulations, we do not have the resolution to achieve that highly turbulent state. The effective Reynolds number of our simulations can be estimated by examining the hydrodynamic drag, for example in the first 20 time units of Fig. 23. This does not quite give enough data to make a good reading, so we ran four simulations with the fiducial parameters ($R = 1, \Delta x/R = 32$), varying u, ($0.125, 0.25, 0.5, 0.75$) and outputting only $u(t)$. An excellent fit to the data is provided by $C_D \approx 0.77$, which corresponds to (see, *e.g.*, Fig. 34 in IV,§45 of Landau and Lifshitz (1987)) a Re of just under 200; even in this more viscous case, the magnetic draping deceleration exceeds the hydrodynamic deceleration by a factor of 2.5.

5.4. Vorticity generation

The flow pattern around a moving body looks as follows for large Reynolds numbers. The flow is laminar and reflects a potential flow solution in almost the entire volume except for a narrow boundary layer and the turbulent wake. The characteristic drag coefficient decreases as the Reynolds number increases (Landau and Lifshitz 1987). This turbulent wake exerts a drag on the body that decelerates it as described in §5.3 and shown in Fig. 22. This figure shows two distinctive deceleration regimes where only the turbulent drag is present in the initial phase, where the magnetic field has not been switched on, and a magnetic tension dominated drag phase at later times.

An independent argument is provided by Fig. 24. In the pure hydrodynamic case, we do not expect any statistical anisotropy of the flow pattern around the moving body. However in our MHD flow, there is an unambiguous anisotropy visible for the stream lines. In the plane perpendicular to the ambient initial magnetic field, the fluid flows smoothly over the projectile with only mild perturbations for streamlines near the boundary layer. In the plane of the initial magnetic field where the draping cone forms, the stream lines are bend towards the turbulent wake and experience the generation of vorticity $\boldsymbol{\omega} = \nabla \times \boldsymbol{v}$. The magnitude of vorticity in our simulations is shown in Fig. 26. Vorticity is generated as the fluid enters the region in the draping layer where magnetic field lines are slipping around the projectile, in particular in the plane transverse to the initial magnetic field. The resulting velocity field can not any more be described by the potential flow solution which causes the analytical solution to break down at the magnetic draping layer and behind the magnetic shoulder. The vorticity in the wake suggests the presence of MHD turbulence that might be responsible for stretching and amplifying the magnetic field furthermore.

We are interested how exactly the topology of the magnetic draping layer can be responsible for generating vorticity into an initially vorticity-free flow pattern. The equation of motion for an

inviscid and magnetized fluid without gravity may be written in the form

$$\rho \frac{\mathrm{d}\boldsymbol{v}}{\mathrm{d}t} = \rho \frac{\partial \boldsymbol{v}}{\partial t} + \rho \left(\boldsymbol{v} \cdot \nabla\right) \boldsymbol{v} = -\nabla P + \boldsymbol{j} \times \boldsymbol{B} = -\nabla\left(P + \frac{B^2}{8\pi}\right) + \frac{1}{4\pi}(\boldsymbol{B} \cdot \nabla)\boldsymbol{B}, \qquad (12)$$

where we define the convective derivative in the first step and applied $\nabla \times \boldsymbol{B} = 4\pi \boldsymbol{j}$ in the last step. The first term on the right-hand side describes the potential force due to the sum of the isotropic thermal pressure P and magnetic pressure $B^2/(8\pi)$, while the second term describes the magnetic tension force. Applying the curl operator to Eqn. (12) and identifying the vorticity $\boldsymbol{\omega} = \nabla \times \boldsymbol{v}$, we arrive at the equation governing the evolution of vorticity:

$$\frac{\mathrm{d}}{\mathrm{d}t}\left(\frac{\boldsymbol{\omega}}{\rho}\right) = \left(\frac{\boldsymbol{\omega}}{\rho} \cdot \nabla\right)\boldsymbol{v} + \frac{1}{4\pi\rho^2} \nabla \times (\boldsymbol{B} \cdot \nabla)\boldsymbol{B} + \frac{1}{\rho^3} \nabla\rho \times \left[\nabla\left(P + \frac{B^2}{8\pi}\right) - \frac{1}{4\pi}(\boldsymbol{B} \cdot \nabla)\boldsymbol{B}\right]. \qquad (13)$$

This equation describes the condition that the vorticity is 'frozen' in the plasma if the last two terms are negligible.[3] Vorticity is necessarily generated, if the curl of the force field generated by magnetic tension does not vanish (referred to as *curl-tension term*). Another source of vorticity is given by a flow where $\nabla\rho$ is not aligned with the potential force due to thermal or magnetic pressure as well as the magnetic tension force (referred to as *baroclinic-type term*). Figure 27 studies the relative importance of both source terms. Due to the large density gradient, the baroclinic-type term dominates the vorticity injection in the magnetic draping layer. The curl of the magnetic tension force seems to be the dominant injection mechanism in the wake. We caution the reader that we cannot quantify the level of vorticity injected by means of a turbulent boundary layer and refer to our phenomenological argument at the beginning of this section that clearly indicates the importance of the magnetic draping layer for the vorticity injection.

6. INSTABILITIES

The magnetic tension force as well as the magnetic layer geometry has implications for the instabilities experienced by the projectile. In §2 and §5, we saw that the flow in the plane parallel to the initial magnetic field is stable and the hydrodynamic instabilities are suppressed by the

---

[3]This can be seen by considering the evolution of an infinitesimal vector $\delta\boldsymbol{x}$ connecting two neighboring fluid parcels, as the fluid moves with the velocity field. The point initially at position $\boldsymbol{x}$ at time t will be displaced to the position $\boldsymbol{x} + \boldsymbol{v}(\boldsymbol{x})\Delta t$ at time $t + \Delta t$. The neighboring point initially at $\boldsymbol{x} + \delta\boldsymbol{x}$ at time t will be displaced to the position $\boldsymbol{x} + \delta\boldsymbol{x} + \boldsymbol{v}(\boldsymbol{x} + \delta\boldsymbol{x})\Delta t$ at time $t + \Delta t$. Hence this 'frozen' connecting line evolves according to

$$\frac{\mathrm{d}}{\mathrm{d}t}(\delta\boldsymbol{x}) = (\delta\boldsymbol{x} \cdot \nabla)\boldsymbol{v}. \qquad (14)$$

which resembles Eqn. (13) if we neglect the last two terms and identify $\delta\boldsymbol{x} = \varepsilon\boldsymbol{\omega}/\rho$ initially, where $\varepsilon > 0$ is a small quantity. Since the differential equation is true for any time, the same relation will hold for all times for the vorticity.

magnetic draping layer (suggested by Dursi 2007). In contrast, the flow around the projectile in the plane transverse to the initial magnetic field is unstable to Kelvin-Helmholtz and Rayleigh-Taylor instabilities, not stabilized by the presence of magnetic field. We will show that the Kelvin-Helmholtz instability remains stronger and leads to gradual disruption of the projectile, although the impact of the Rayleigh Taylor instability in our MHD case is greater than the purely hydrodynamical case because of the greater deceleration. For an homogeneous initial magnetic field the induced vorticity remains largely two-dimensional.

The projectile is being decelerated by magnetic tension as shown in §5.3. This makes the projectile subject to *Rayleigh-Taylor instabilities* with a characteristic frequency (Chandrasekhar 1981)

$$\omega_{\mathrm{RT}}^2 = \frac{\langle \rho_{\mathrm{p}} \rangle - \rho_0}{\langle \rho_{\mathrm{p}} \rangle + \rho_0} \, \dot{u}_{\mathrm{T}} \, k \simeq \frac{3}{8} \frac{2\pi \, \rho_0 \, C_{\mathrm{G}}}{\langle \rho_{\mathrm{p}} \rangle} \frac{u^2}{R^2} \frac{k}{k_0} \geq \frac{3\pi \, \rho_0 \, C_{\mathrm{G}}}{4 \langle \rho_{\mathrm{p}} \rangle} \frac{u^2}{R^2}, \tag{15}$$

where $k_0 = 2\pi/R$ defines the the smallest wavenumber of the system and we work in the limit where $\langle \rho_{\mathrm{p}} \rangle \gg \rho_0$.

The flow around the projectile causes a shear at the interface of the projectile that can get non-linear by means of the *Kelvin-Helmholtz instability* and has the characteristic frequency (Chandrasekhar 1981)

$$\omega_{\mathrm{KH}} = \frac{\sqrt{\langle \rho_{\mathrm{p}} \rangle \rho_0}}{\langle \rho_{\mathrm{p}} \rangle + \rho_0} \, \Delta u \, k \simeq \frac{3\pi \, u}{R} \sqrt{\frac{\rho_0}{\langle \rho_{\mathrm{p}} \rangle}} \frac{k}{k_0} \geq \frac{3\pi \, u}{R} \sqrt{\frac{\rho_0}{\langle \rho_{\mathrm{p}} \rangle}}. \tag{16}$$

Here we neglect the self-gravity of the projectile and apply the maximal velocity shear from the potential flow solution around a spherical body, $v = 3/2 \, u \, \mathbf{e}_\theta$, which is valid at $r = R$ and $\theta = \pi/2$.

Which instability will eventually dominate and set the relevant timescale? It turns out that the ratio of the characteristic frequencies is independent of the projectile properties and only depends on the wave number of the considered mode,

$$\frac{\omega_{\mathrm{KH}}^2}{\omega_{\mathrm{RT}}^2} \simeq \frac{12\pi}{C_{\mathrm{G}}} \frac{k}{k_0} \geq \frac{12\pi}{C_{\mathrm{G}}} \simeq 20. \tag{17}$$

where from the previous section, $C_{\mathrm{G}} \approx 1.87$ takes into account the fact that both the magnetic field strength and radius of curvature of the field lines vary over the 'cap' of the projectile. The largest length scale of the problem is given by the size of the projectile in the direction of motion and sets the largest timescale of the problem,

$$\frac{T_{\mathrm{KH}}}{T_{\mathrm{RT}}} \simeq \frac{1}{2} \sqrt{\frac{C_{\mathrm{G}} \, k_0}{3\pi \, k}} \leq 0.22. \tag{18}$$

Thus, we expect the Kelvin-Helmholtz instability in the plane transverse to the initial magnetic field to be responsible for the eventual disintegration of the projectile. These considerations allow us to

estimate the associated time- and length-scale on which we expect to see the projectile material in the boundary layer to become unstable,

$$L_{KH} = T_{KH}\,u = \frac{2\pi\,u}{\omega_{KH}} \simeq \frac{2R}{3}\sqrt{\frac{\langle\rho_p\rangle}{\rho_0}}\frac{k_0}{k} \le \frac{2R}{3}\sqrt{\frac{\langle\rho_p\rangle}{\rho_0}} \simeq 16.3 \qquad (19)$$

in terms of the length units in the code. This explains nicely the instability features in the wake of Fig. 28 that appear every 10 length units and indicate that a mode that is slightly smaller than the projectile dimension is becoming unstable and leads to a deposition of projectile material.

7. DISCUSSION AND LIMITATIONS

We have investigated in detail the rapid formation of a magnetic draping layer over a projectile, and examined some of the immediate dynamical consequences. It is worth considering how well these insights continue to hold over longer timescales, and whether the draped field can offer much protection over significant distances.

While details of how mixing might take place will depend sensitively on the structure of the object in question, one requirement for a projectile to mix significantly into the surrounding medium will be for the projectile to sweep past on order its own mass in the ambient medium; only then will there have been enough shear to significantly disrupt the moving object. This requires the projectile to traverse a distance $L \sim (\langle\rho_p\rangle/\rho_0)R$. For the runs considered in previous sections, modeling this while continuing to resolve the magnetic draping layer would require extremely costly simulations, even with AMR.

However, at the cost of complicating direct comparison with previous simulations, one can gain some insight into what will happen over longer times by considering those regions of parameter space which make the computation more feasible. In particular, for this section we perform an analog to run B made with a maximum projectile density reduced by a factor of 10, so that $\langle\rho_p\rangle/\rho_0 \approx 15$. With this reduced density contrast, mixing happens more easily and the projectile sweeps past its own mass in a computationally approachable time. Results from this run are shown in Fig 29, at a time when the projectile has approximately swept through its own mass of ambient medium.

In this run, the same features are seen as in previous sections; the development of the strong narrow magnetic field layer, the opening angle $\sim v_A/u$, and the large-scale vorticity oriented primarily along field lines generated in the wake. However, over long times the anisotropy imposed by the direction preferred by the magnetic field, and as suggested in Fig.4, becomes much more pronounced, as the projectile becomes extremely aspherical; it is greatly flattened along the direction of the magnetic field lines.

The long-time distortion of the projectile by the magnetic field – which, again, is initially strongly subthermal ($\beta \sim 100$) and a factor of 6 less than the ram pressure seen by the projectile – is particularly evident when seen compared to the results of the same projectile moving in the absence of a magnetic field, as in Fig. 30. In this case, density is plotted in two cut planes at the same time for the simulation with and without magnetic field. Three dimensional interactive density isosurfaces are also plotted in Fig. 31.

Several features are immediately apparent. The first is the significantly different density distributions between the two scenarios. The densest material is more contained in the case with magnetic draping, but in the plane along the magnetic field, material which is stripped off is more extended, piling up along the draped magnetic contact. The plane across the initial magnetic field lines is even more interesting; here the stripped material is much more contained, even with the presence of the Kelvin-Helmholtz instability. Here stripped material stays almost completely within a cylinder of radius $R = 1$, the initial radius of the projectile, along the path of the projectile.

Also evident is that, although the two simulations are examined at the same time, the projectile without magnetic fields is significantly further ahead in the domain than the simulation with the magnetic field; this is the result of the deceleration demonstrated in § 5.3.

In this work we have made several simplifying assumptions to allow us to begin to understand the process of the draping. We have neglected consideration of the interior structure of the projectile, by for instance omitting any self gravity which would be relevant for a minor merger. This will effect the rate of stripping of material off of the core, and thus long-term evolution, but is unlikely to directly effect the draping process itself. We have also not considered any gradient of properties in the medium the projectile moves through; while this again would effect long term behaviour, the set-up of the magnetic draping layer occurs so quickly that it is unlikely that any background quantities would greatly change over the small distances involved.

We have also omitted explicit treatment of dissipative microphysics Lyutikov (2007); Schekochihin et al. (2007). Following up with simulations which included these effects self-consistency will be important for examining in detail the resulting sharpness of the cold fronts (as done, for example, by Asai et al. (2006)) and the different dissipation physics may also well effect the long time behaviour of mixing. However, the initial draping layer is set up, and its properties are determined, on timescales much faster than the dissipative timescales, so these results will be unaffected.

We have also considered here only subsonic motions through the ambient medium. Many of the astrophysical processes where draping is relevant can be supersonic, and so an important next step is to consider this case, where a bow shock will occur before the magnetic draping layer. While the bow shock will almost certainly be well separated from the magnetic draping layer, the shock will affect both the geometry of the flow onto the draping layer and greatly amplify the

importance of the thermal pressure. On the other hand, behind the bow shock the flow will be subsonic, so much of the discussion here will directly apply. Similar detailed studies of draping in the supersonic case will be considered in future work. Perhaps more seriously, we have considered here only the simplest case of an initial magnetic field uniform over the scales of interest. It will be necessary to consider more realistic field geometries. This, too, is being considered in future work, and will require much more careful treatment of the detailed magnetic structure of the field.

8. CONCLUSION

This work aims at understanding the morphology and the dynamical properties of magnetic draping to set a solid ground for its astrophysical applications. A core, bullet, or bubble that moves super-alfvénically in even a very weakly magnetized plasma necessarily sweeps up enough magnetic field to build up a dynamically important sheath around the object; the layer's strength is set by a competition between 'plowing up' of field and field lines slipping around the core, and to first order depends only on the ram pressure seen by the moving object. This layer is developed very quickly, potentially faster than a crossing time of the projectile. The energy density in the draped layer, at its maximum, exceeds the ram pressure by a factor of two, necessary to anisotropically redirect the flow. This effect has important implications for galaxy cluster physics as it suppresses hydrodynamic instabilities at the interface of AGN bubbles. It naturally explains so-called 'cold fronts' by keeping temperature and density interfaces of merging cores sharp that would otherwise be smoothed out by thermal conduction and diffusion. Other important astrophysical implications of this effect include draping of the solar wind magnetic field at the bow shock of the Earth as well as pulsar wind nebulae.

In this paper, we compare a simplified analytical solution of the problem that neglects the back-reaction of the dynamically important magnetic field on the potential flow with a high-resolution AMR simulation and find very good agreement between both solutions in the region ahead of the bubble. Non-linear back-reaction of the magnetic field in the draping layer necessarily implies the generation of vorticity in the flow. The induced vortices in the wake deform the core hydrodynamically and eventually cause the magnetic sheath to peel off. There is a strong indication that the vorticity generation is responsible for the intermittent amplification and stretching of the magnetic fields as well as the injection of MHD turbulence in the wake of the core. If this withstands further critical analysis, this mechanism might have profound astrophysical implications for the amplification and generation of large-scale magnetic fields in the inter-galactic medium.

The magnetic layer, once fully developed, has a characteristic geometry which we have shown here to be roughly conical in the plane along the magnetic field lines, with opening angle $\theta \sim \arctan(v_A/u)$, and remains contained in the perpendicular plane, with the Kelvin-Helmholtz

instability acting on the object interface. The magnetic tension in the layer significantly decelerates the object, dominating over any hydrodynamic drag.

Over long times, the anisotropy imposed by the field – despite the fact that the field is initially highly subthermal and with an energy density significantly less than the kinetic energy of the ambient medium in the frame as the projectile – can significantly distort the projectile, keeping it significantly more constrained in the plane perpendicular to the ambient field, and keeping any stripped material inside the drape.

If a magnetic draping layer such as generated in these simulations were astrophysically observable, it would be possible to get independent measurements of the magnetic field strength in the ambient medium provided the local gas density and the velocity of the moving object is known. The tools are both the opening angle of the drape and the thickness of the magnetic field layer – but not through the layer's field strength. Similarly, for a known magnetic field strength, we would have an alternate measure of the velocity of the projectile.
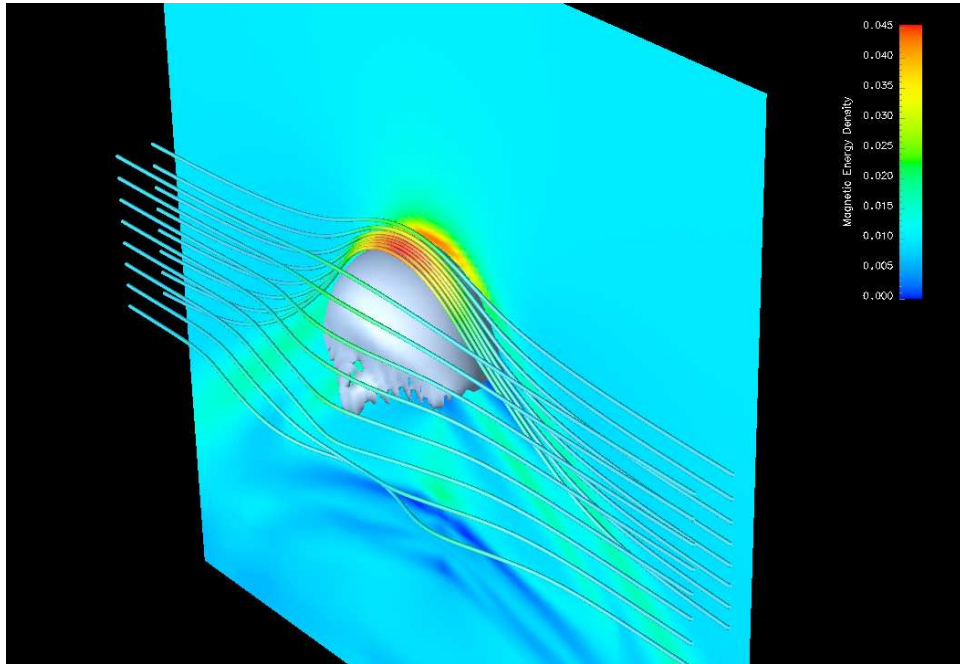
– 36 –

Fig. 16.— As in Fig. 1, but for Run E; that is, with the projectile's velocity reduced by a factor of one-half (so that $u = 0.125$ in code units).

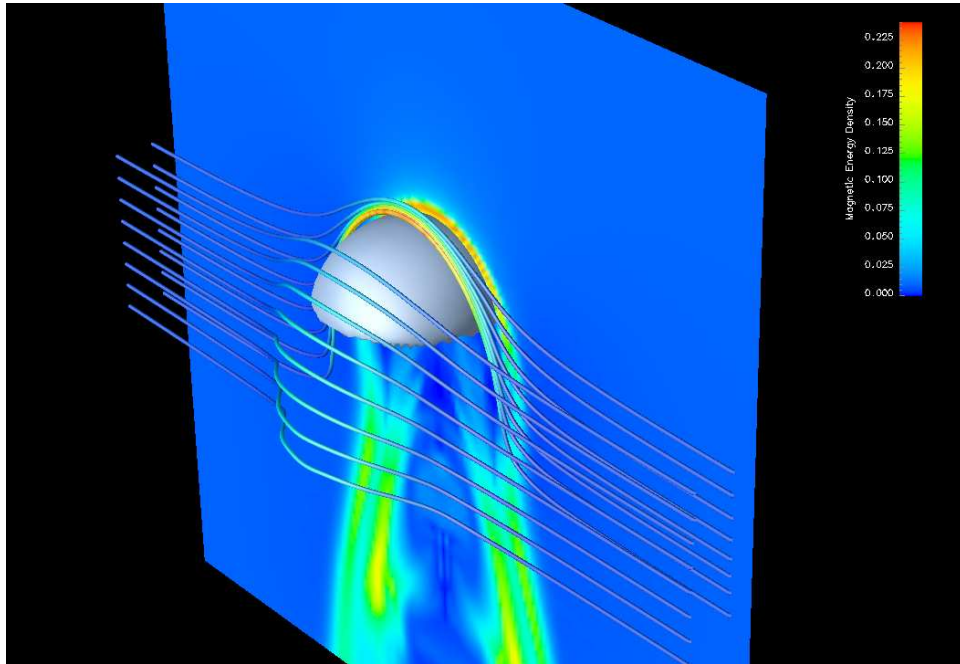Fig. 17.— Interactive 3D version of Figure 16 above.

Fig. 18.— As in Fig. 1, but for run G; that is, with the projectile's velocity increased by a factor of two (so that $u = 0.5$ in code units).

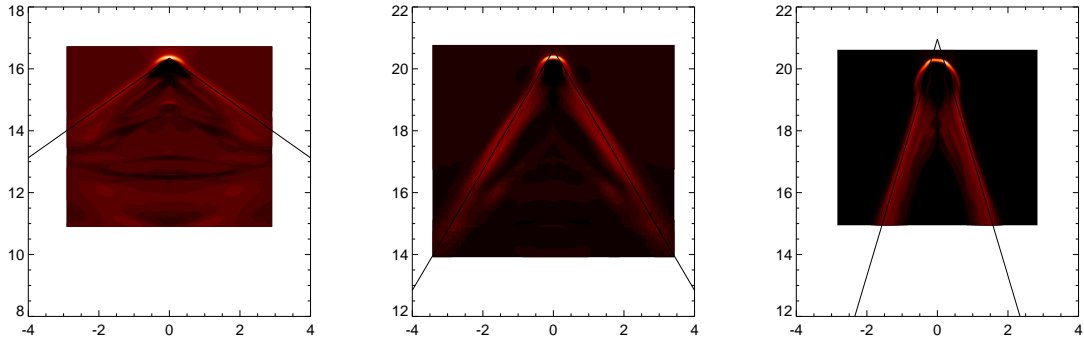Fig. 19.— Interactive 3D version of Figure 18 above.

Fig. 20.— Plot of magnetic energy density in the y,z plane for simulations with $R = 0.5$ and, left to right, $u = 0.125, 0.25, 0.5$; shown with black lines are the fitted opening angles of the magnetic draping layer, omitting the region including the material from the projectile. The fit slopes (*e.g.*, $\tan\theta$) are 1.24, 0.515, 0.261, and those predicted by $v_{A0}/\langle u \rangle$ are 1.13, 0.566, 0.283; this agreement is within 10%.
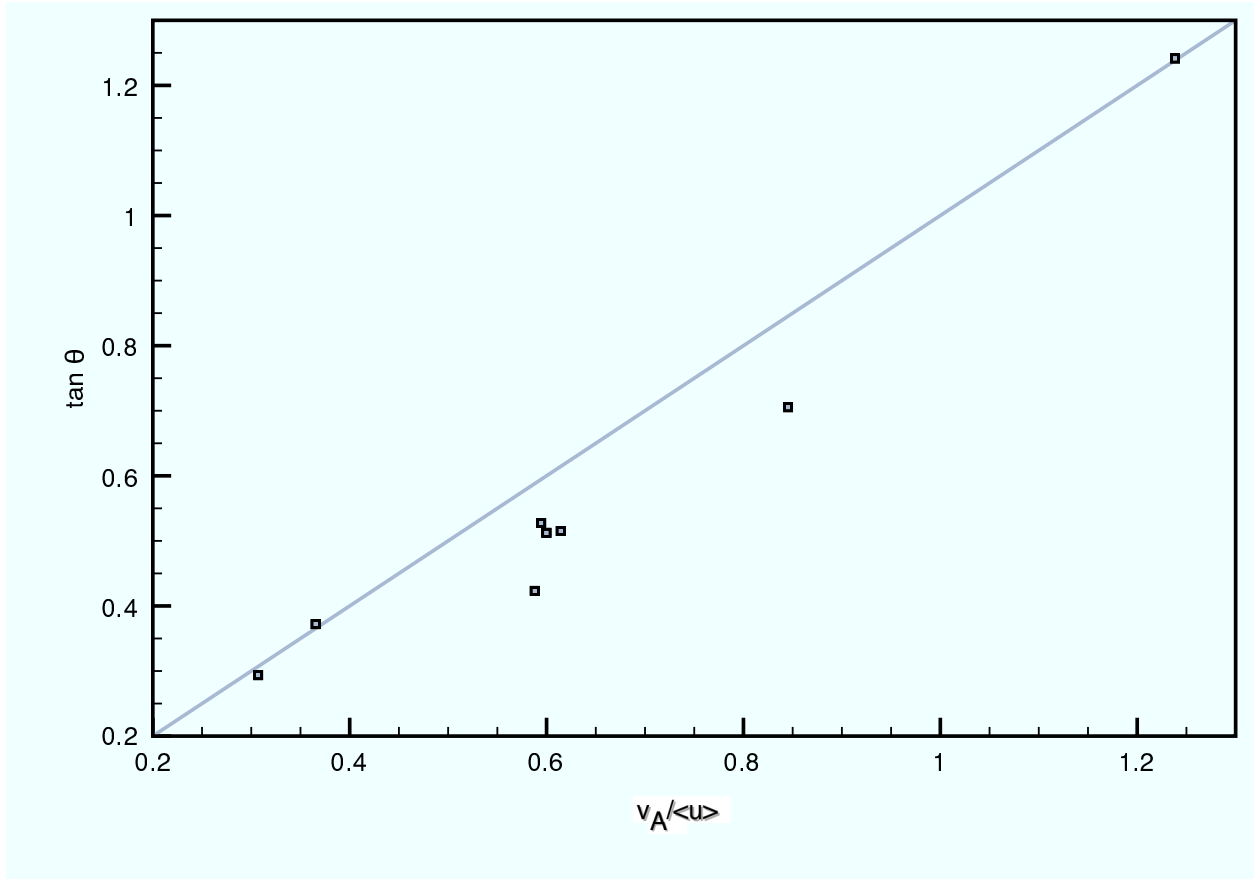
Fig. 21.— A plot for the 3d runs presented here showing the tangent of the fit opening angles of the drape in the yz plane versus $v_A/\langle u \rangle$. Data from all runs are shown.
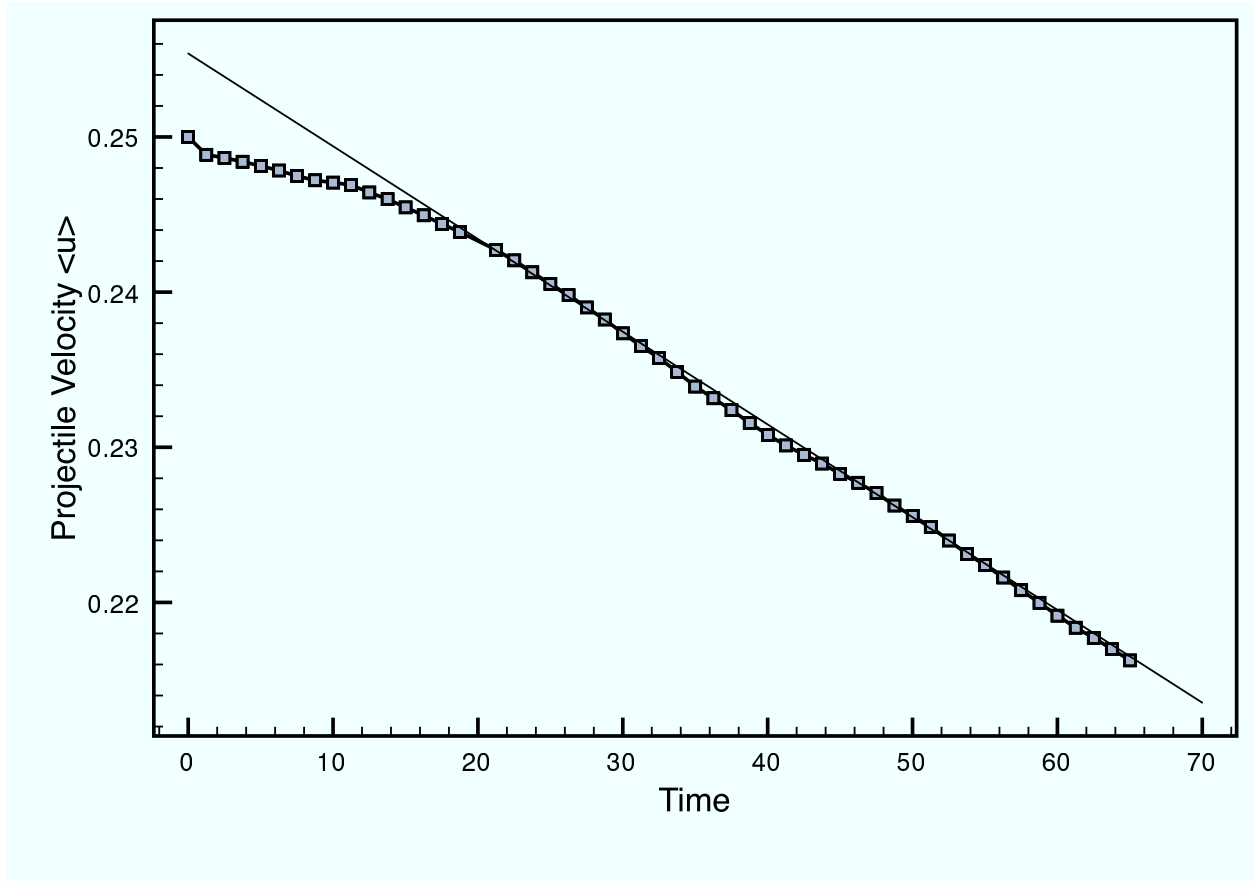
Fig. 22.— A plot showing, with squares, the evolution of projectile velocity (calculated as in by Eqn.9) over time for run F. Note that the projectile encounters the magnetic field at time 20 in these units. Plotted as a thin line is the best fit deceleration, $\dot{u} = -5.98 \times 10^{-4}$, for times greater than 20.
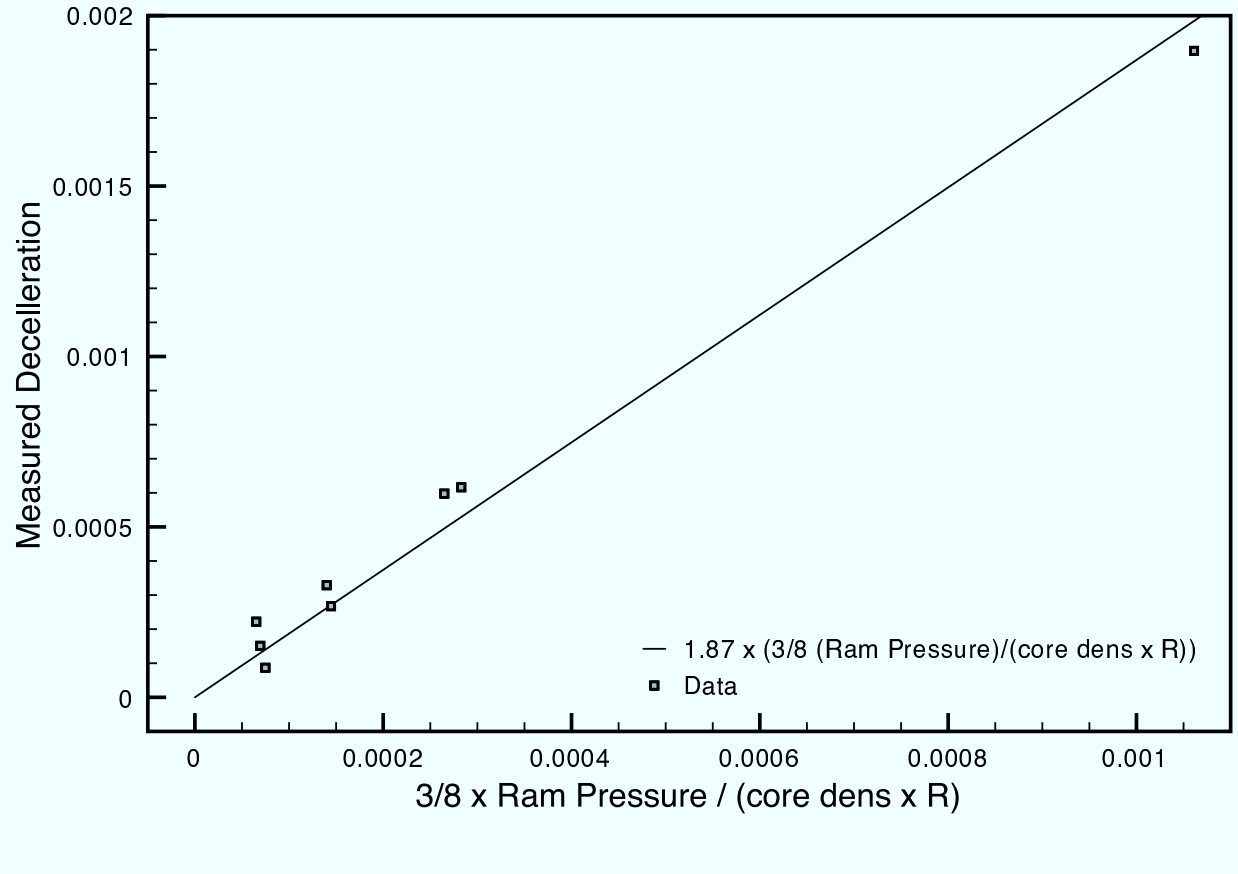
Fig. 23.— A plot for the 3d runs presented here showing the measured deceleration of the projectile versus the functional form we expect it to take, proportional to $3/8\rho u^2/(\langle\rho_p\rangle R)$, where $\langle\rho_p\rangle$ is the mean density of the projectile (in code units, ≈ 150). Because the magnetic field strength and curvature varies over the draped layer, there is an undetermined geometrical factor in the magnitude of the deceleration; we find it here to be approximately 1.87.
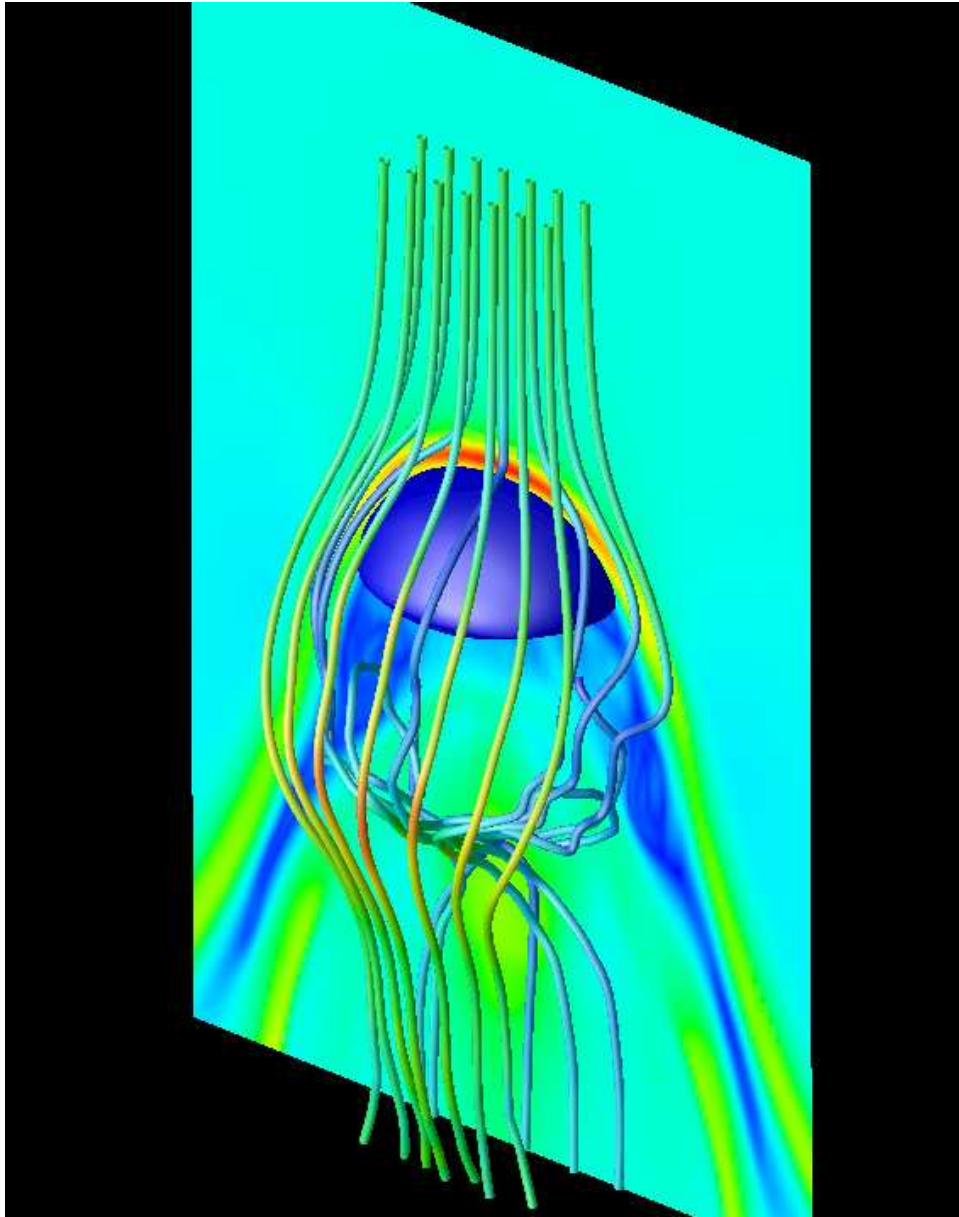
Fig. 24.— Plot of streamlines over the $R = 2$ projectile through a $\beta = 100$ medium. Streamlines are calculated in the frame of the mean velocity of the projectile. The streamlines are coloured by the magnitude of velocity, and the plane is once again colored by magnetic energy density. At this time, no instabilities have developed in the plane perpendicular to the ambient magnetic field, so fluid flows smoothly over the projectile in this plane; however, fluid traveling close to the other plane experience a gain of vorticity.

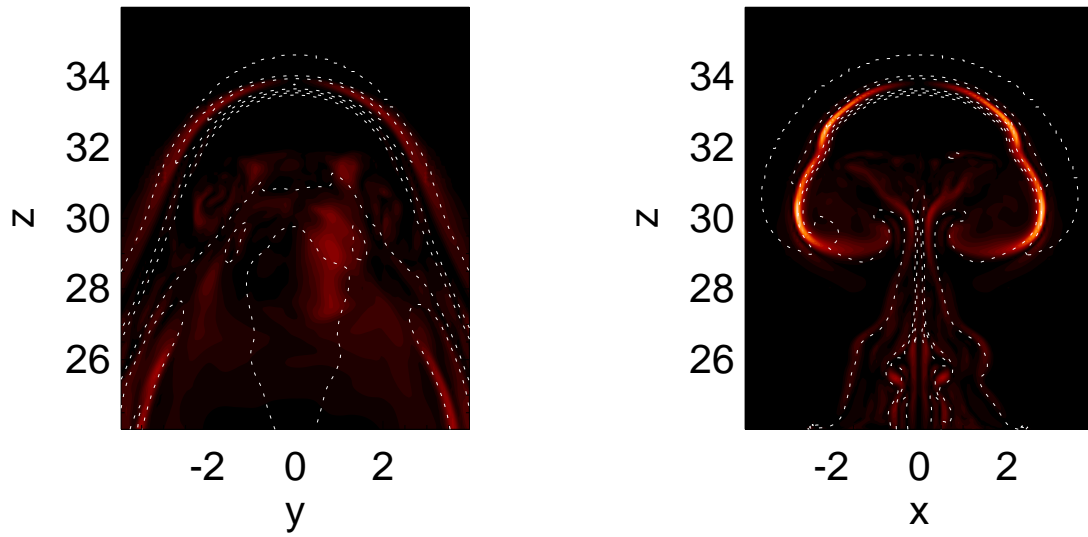Fig. 25.— Interactive 3D version of Figure 24 above.

Fig. 26.— The magnitude of vorticity is shown in color in the plane parallel and transverse to the initial magnetic field (left and right panel). The dotted lines represent iso-density contours. The magnetic energy density is shown in the contour plot. Vorticity in the draping layer is generated predominantly by a baroclinic-type term whereas the vorticity injection in the wake is dominated by the curl of the magnetic tension force.
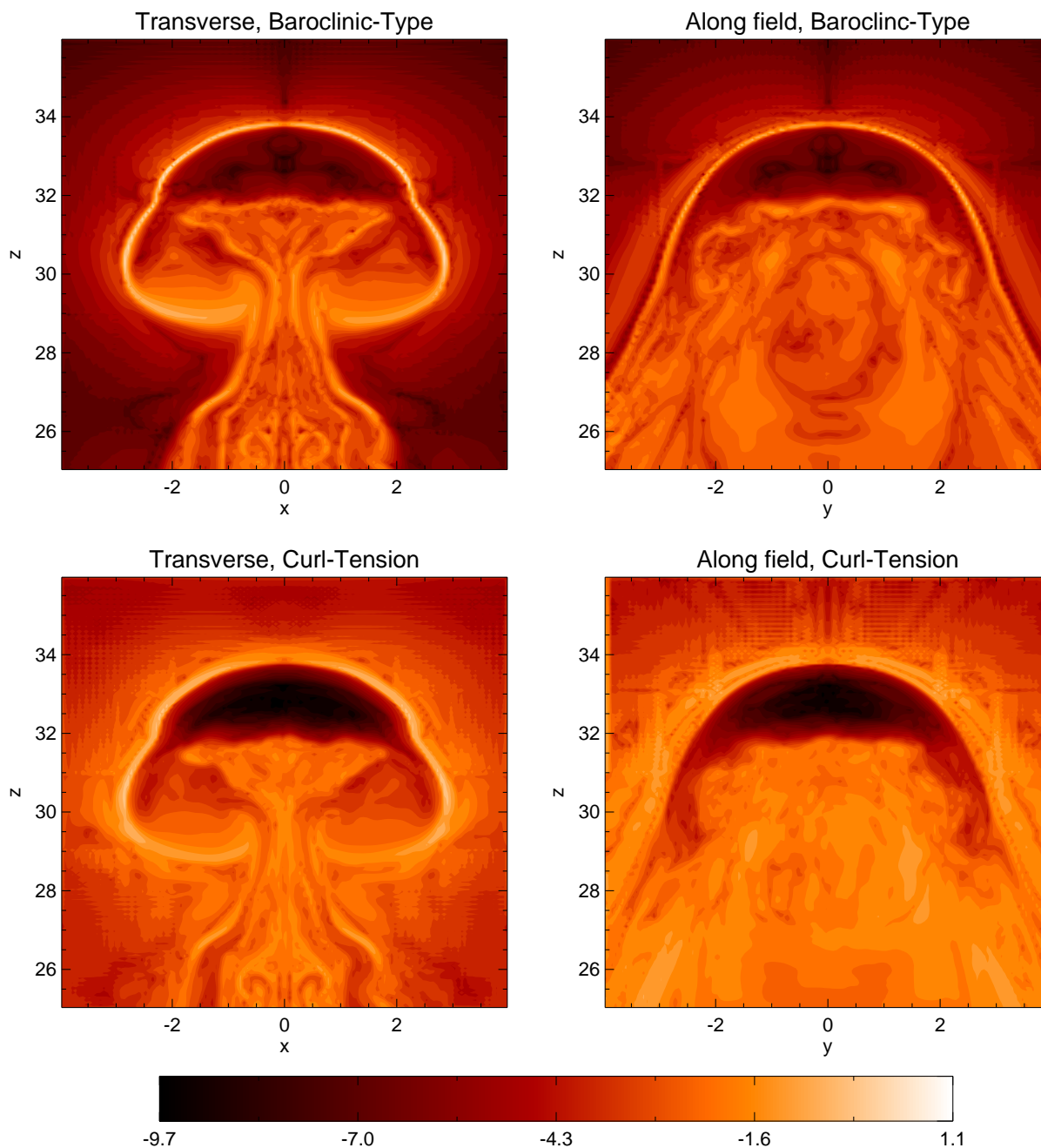
Fig. 27.— Plot of the source terms for the specific vorticity injection rate as defined in Eqn. 13 for the plane transverse/parallel to the initial magnetic field (left/right panels). The upper panels show the contribution of the baroclinic-type term where $\nabla\rho$ is not aligned with the thermal and magnetic pressure force. Due to the large density gradient, this term dominates the vorticity injection in the magnetic draping layer as we verified with a linear color scale. The curl of the magnetic tension force seems to be the dominant injection mechanism in the wake.
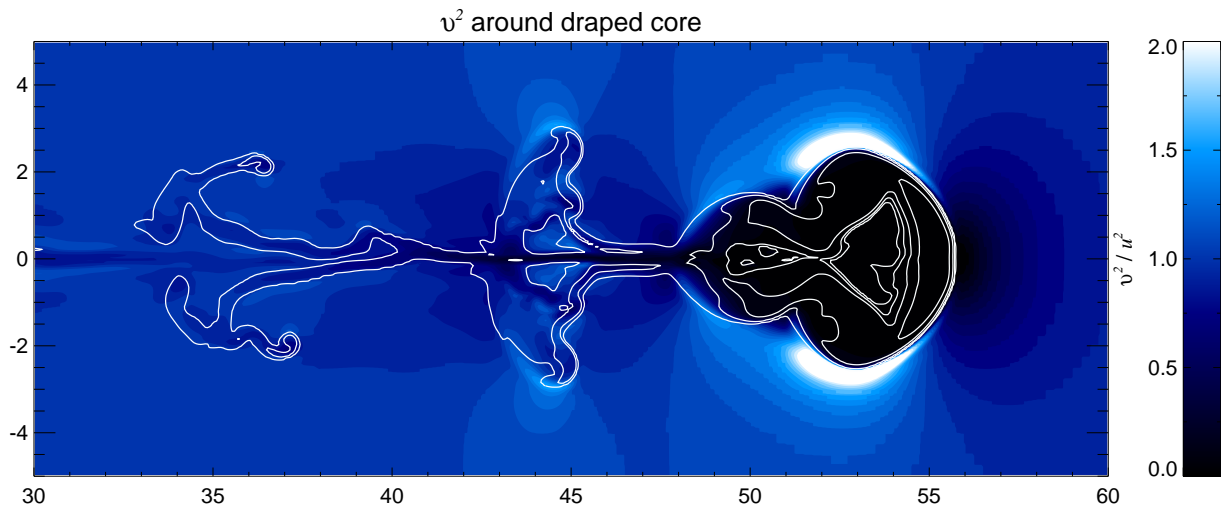
Fig. 28.— Kelvin-Helmholtz instability dissolves the projectile in the plane perpendicular to the initially homogeneous magnetic field. The flow is accelerated at the density enhancements of the stripped material due to the Bernoulli effect. In the wake of the projectile, there is a characteristic length scale of ~ 10 length units between the striped material which corresponds to an unstable mode with a wavelength of $2/3R$.
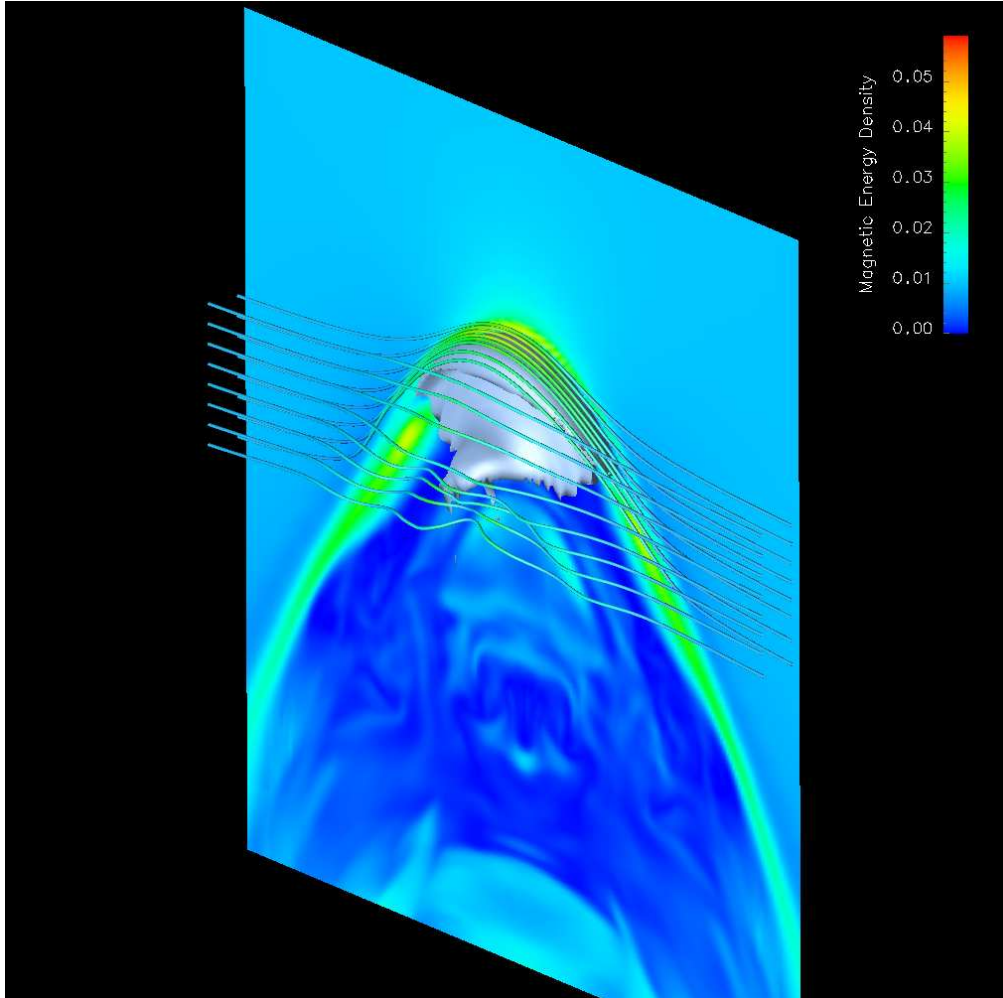
Fig. 29.— As in Fig. 1, but for the $\langle \rho_p \rangle = 15$ run, at a time where the projectile has swept past approximately its own mass in ambient fluid.
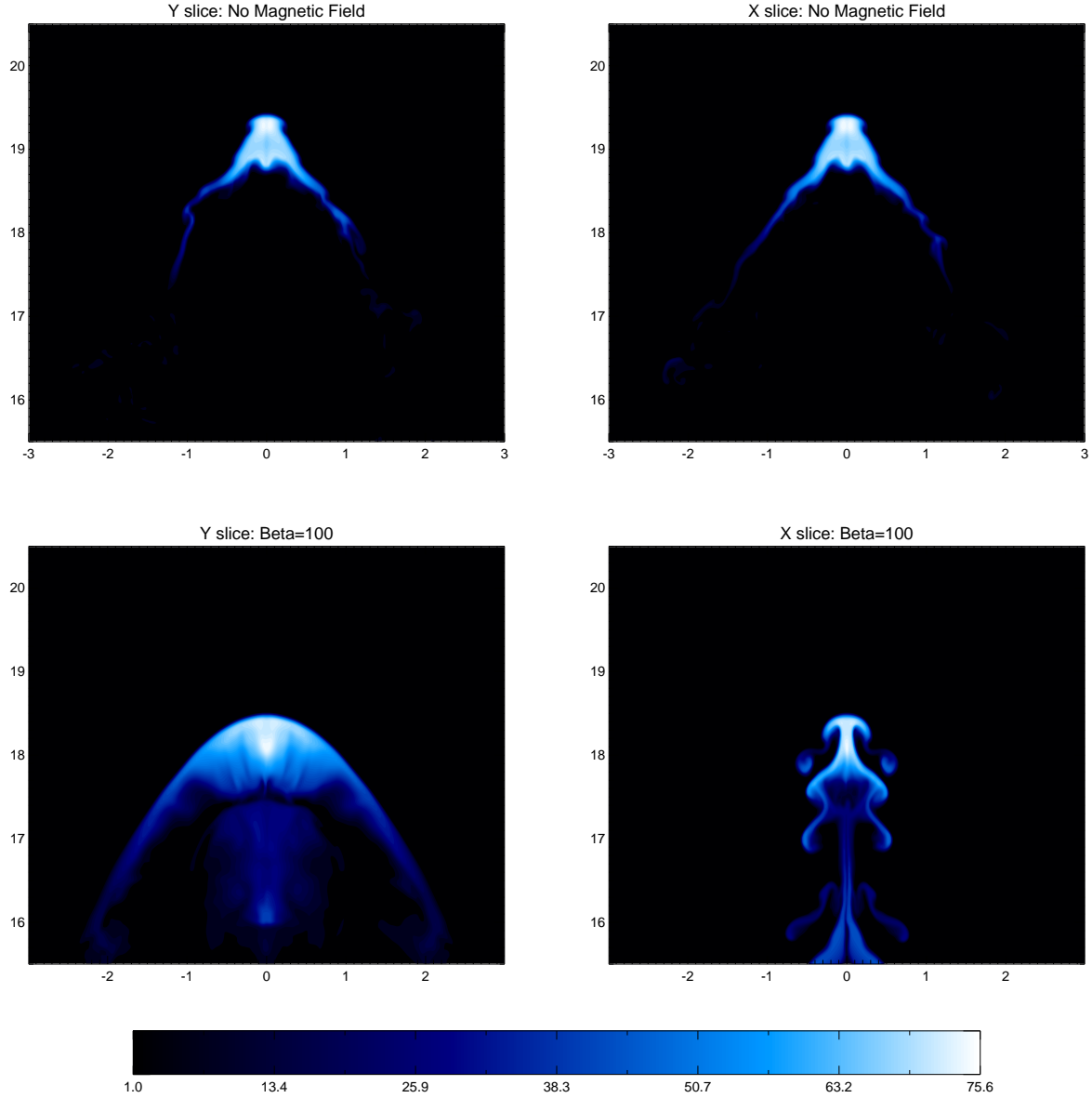
Fig. 30.— Plots of density shown for the $\langle\rho_{\rm p}\rangle/\rho_0 = 15$ run, at a time when the projectile has swept past roughly its own mass of ambient medium. Shown at top are simulations with no initial magnetic field, and at bottom which a magnetic field as in Run B, with $\beta = 100$ and $\rho_0 u^2/P_{b,0} = 6.25$. Panels on the left are along the y direction (*e.g.*, the direction of the initial magnetic field lines in the second case) and along the x direction (perpendicular to the magnetic field lines) on the right. These snapshots are taken at the same simulation time for the two runs; the projectile in the magnetized case lags because of the deceleration demonstrated in § 5.3.

Fig. 31.— Interactive 3D version of Figure 30 above

.

A. DERIVATION OF THE MHD FLOW AROUND A MOVING BODY

A.1. The exact MHD solution

The full non-linear solution of the MHD flow around a moving and dynamically evolving body is extremely complex because of its significant three-dimensionality and non-linearity. Owing to the range of scales involved this problem is perfectly suited for an MHD adaptive mesh refinement simulation. In order to gain credibility and improve our understanding of the properties of the numerical solution including its scaling behavior, we solve the problem of an ideally conducting plasma around a spherical body analytically. To this end, we solve for the flow of a plasma with a frozen-in magnetic field around a sphere to explore the characteristics of the magnetic field near the surface of the body. We disregard any possible change in the flow pattern by means of the back-reaction of the magnetic field. The same problem has been investigated by Bernikov and Semenov (1980) who find that the energy density of the magnetic field forming in the wake behind the body diverges logarithmically. In passing by we correct the misconception that lead to this unphysical behavior of their solution and derive a criterion for the breakdown of our simplified analytical solution that we then successfully apply to our numerical solution.

The governing equations of ideal MHD with infinity conductivity are given by

$$\mathrm{curl}(\boldsymbol{v} \times \boldsymbol{B}) = \boldsymbol{0} \quad \text{and} \quad \mathrm{div}\,\boldsymbol{B} = 0. \tag{A1}$$

We solve this system of equations outside the sphere for a given velocity field that is derived for a viscous and incompressible flow around the sphere. Without loss of generality, we choose the origin of our spherical coordinate system to coincide with the center of the sphere with radius R (Fig. 1) and the z-axis being anti-parallel to the fluid velocity at infinity. The potential flow solution of the pure hydrodynamical problem reads in spherical coordinates as follows (Kotschin et al. 1954):

$$\boldsymbol{v} = \boldsymbol{e}_r \left(\frac{R^3}{r^3} - 1 \right) u \cos\theta + \boldsymbol{e}_\theta \left(\frac{R^3}{2r^3} + 1 \right) u \sin\theta = -\boldsymbol{u} + \frac{R^3}{2r^3} \left[3\boldsymbol{e}_r(\boldsymbol{u} \cdot \boldsymbol{e}_r) - \boldsymbol{u} \right], \tag{A2}$$

where we employed the coordinate independent representation of the homogeneous fluid velocity at infinity in the second step, $\boldsymbol{u} = \boldsymbol{e}_r(\boldsymbol{u} \cdot \boldsymbol{e}_r) + \boldsymbol{e}_\theta(\boldsymbol{u} \cdot \boldsymbol{e}_\theta)$. Since for any stream line holds $\mathrm{d}r/v_r = r\mathrm{d}\theta/v_\theta$, we can thus derive the equation of the line of flow using Stoke's method of the stream function

$$p = r \sin\theta \sqrt{1 - \frac{R^3}{r^3}}, \tag{A3}$$

where p is the impact parameter of the given line of the flow from the z-coordinate axis on an infinitely distant plane in the left half-space. We assume a homogeneous magnetic field at infinity in the left half-space pointing towards the positive y-coordinate axis yielding the boundary conditions for $\boldsymbol{B}$:

$$B_r|_\infty = B_0 \sin\theta \sin\phi, \quad B_\theta|_\infty = B_0 \cos\theta \sin\phi, \quad B_\phi|_\infty = B_0 \cos\phi. \tag{A4}$$

Writing Eqns. (A1) for the components yields

$$\text{curl}_r(\boldsymbol{v} \times \boldsymbol{B}): \quad \frac{\partial}{\partial \theta}[\sin\theta(v_r B_\theta - v_\theta B_r)] + \frac{\partial}{\partial \phi}(v_r B_\phi) = 0, \tag{A5}$$

$$\text{curl}_\theta(\boldsymbol{v} \times \boldsymbol{B}): \quad \frac{\partial}{\partial r}[r(v_r B_\theta - v_\theta B_r)] - \frac{1}{\sin\theta}\frac{\partial}{\partial \phi}(v_\theta B_\phi) = 0, \tag{A6}$$

$$\text{curl}_\phi(\boldsymbol{v} \times \boldsymbol{B}): \quad \frac{\partial}{\partial r}(r v_r B_\phi) + \frac{\partial}{\partial \theta}(v_\theta B_\phi) = 0, \tag{A7}$$

$$\text{div}\boldsymbol{B}: \quad \frac{1}{r^2}\left[\frac{\partial}{\partial r}\left(r^2 B_r\right)\right] + \frac{1}{r\sin\theta}\left[\frac{\partial}{\partial \theta}(\sin\theta B_\theta)\right] + \frac{1}{r\sin\theta}\frac{\partial B_\phi}{\partial \phi} = 0. \tag{A8}$$

By substituting (A2) into (A7) we obtain the equation for B_ϕ

$$\frac{\partial}{\partial r}B_\phi + \frac{v_\theta}{r v_r}\frac{\partial}{\partial \theta}B_\phi = -\frac{3 B_\phi R^3}{2r(r^3 - R^3)}, \tag{A9}$$

where $v_\theta/(r v_r) = -\tan\theta\,(2r^3 + R^3)/[2r(r^3 - R^3)]$. Equation (A9) is a linear inhomogeneous first-order partial differential equation which can be solved by the method of characteristics. We take r as parameter in the characteristic equations and express the variables θ and ϕ in terms of r, using

$$\frac{\mathrm{d}B_\phi}{\mathrm{d}r} = \frac{\partial B_\phi}{\partial r} + \frac{\partial B_\phi}{\partial \theta}\frac{\partial \theta}{\partial t}\frac{\partial t}{\partial r} + \frac{\partial B_\phi}{\partial \phi}\frac{\partial \phi}{\partial t}\frac{\partial t}{\partial r} = \frac{\partial B_\phi}{\partial r} + \frac{v_\theta}{r v_r}\frac{\partial B_\phi}{\partial \theta}. \tag{A10}$$

Thus, on the line of the flow that is uniquely characterized by its impact parameter p at infinity, we obtain a first order ordinary differential equation for B_ϕ,

$$\frac{\mathrm{d}B_\phi}{\mathrm{d}r} = -\frac{3 B_\phi R^3}{2r(r^3 - R^3)}. \tag{A11}$$

Integrating this equation by the separation of variables yields the solution for B_ϕ that contains a constant which is determined from the homogeneous magnetic field at infinity (A4),

$$B_\phi = \frac{B_0 \cos\phi}{\sqrt{1 - \dfrac{R^3}{r^3}}}. \tag{A12}$$

To determine B_r and B_θ, we turn to Eqns. (A5) and (A6). By multiplying Eqn. (A5) with r and (A6) with $\sin\theta$, defining $K \equiv r\sin\theta(v_r B_\theta - v_\theta B_r)$, and combining (A6) and (A5), we obtain the equation for K:

$$\frac{\partial K}{\partial r} + \frac{v_\theta}{r v_r}\frac{\partial K}{\partial \theta} = 0. \tag{A13}$$

Equation (A13) can again be solved by the method of characteristics as (A9) yielding $K = K_p$, where K_p is a constant on each flow line that is labeled with its impact parameter p. Determining

this constant from Eqn. (A4) and substituting for K and K_p their values, we obtain the following equation that relates B_r and B_θ,

$$r \sin \theta \, (\upsilon_r B_\theta - \upsilon_\theta B_r) = -puB_0 \sin \phi. \tag{A14}$$

Substituting B_θ, expressed in terms of B_r, from Eqn. (A14) and B_ϕ from Eqn. (A12) into the solenoidal condition for $\boldsymbol{B}$ (A8), we obtain the equation for B_r. Similarly, substituting B_r, expressed in terms of B_θ and following the same steps, leads to the equation for B_θ:

$$\frac{\partial B_r}{\partial r} + \frac{\upsilon_\theta}{r\upsilon_r} \frac{\partial B_r}{\partial \theta} + \left[\frac{2}{r} - \frac{2r^3 + R^3}{2r(r^3 - R^3)} \left(1 + \frac{1}{\cos^2 \theta} \right) \right] B_r = -\frac{B_0 \sin \phi \sin \theta}{r \sqrt{1 - \frac{R^3}{r^3} \cos^2 \theta}}, \tag{A15}$$

$$\frac{\partial B_\theta}{\partial r} + \frac{\upsilon_\theta}{r\upsilon_r} \frac{\partial B_\theta}{\partial \theta} + \left[\frac{2}{r} - \frac{2r^3 + R^3}{2r(r^3 - R^3)} + \frac{9r^2 R^3}{(2r^3 + R^3)(r^3 - R^3)} \right] B_\theta =$$

$$\frac{2B_0 \sin \phi \, (r^3 + 2R^3)}{r \cos \theta \, (2r^3 + R^3) \sqrt{1 - \frac{R^3}{r^3}}}. \tag{A16}$$

Both equations can again be solved by the method of characteristics, expressing the variables θ and ϕ in terms of r which we take to be the independent parameter along the flow lines and using Eqn. (A3). Note that for a potential flow, the variable ϕ is always constant on the line of the flow by symmetry. The resulting linear inhomogeneous first-order ordinary differential equations are easily solved by an integrating factor that is derived from the homogeneous equations, leading to the solutions for B_r and B_θ,

$$B_r = \frac{r^3 - R^3}{r^3} \cos \theta \left[C_1 \mp B_0 \sin \phi \int_\xi^r \frac{p(r,\theta) r'^4 \, \mathrm{d}r'}{(r'^3 - R^3 - p(r,\theta)^2 r')^{3/2} \sqrt{r'^3 - R^3}} \right], \tag{A17}$$

$$B_\theta = \frac{2r^3 + R^3}{r^{5/2} \sqrt{r^3 - R^3}} \left[C_2 \pm 2B_0 \sin \phi \int_\xi^r \frac{r'^3 (r'^3 + 2R^3) \sqrt{r'^3 - R^3} \, \mathrm{d}r'}{(2r'^3 + R^3)^2 \sqrt{r'^3 - R^3 - p(r,\theta)^2 \, r'}} \right], \tag{A18}$$

where C_1 and C_2 are integration constants and ξ is the initial value for which B_r and B_θ are known. The upper signs refer to the region $0 \le \theta \le \pi/2$, and the lower signs to $\pi/2 \le \theta \le \pi$.

A.2. The approximate MHD solution near the sphere

We aim at understanding the behavior of the magnetic field in the region near the sphere. To this end, we investigate the behavior of the integrals in (A17) and (A18) for small impact parameters and keep only the main terms with respect to p. We find that the integral in (A17) diverges at the lower limit logarithmically for $\pi/2$ and the integral in (A18) has a linear divergence

at the lower limit. Thus we will use (A17) in the region $0 \le \theta \le \pi/2$ and (A18) in the region for $\pi/2 \le \theta \le \pi$.

We divide the region of integration into two: the first from ∞ to r_1 where $r_1 > R$ is the radius of the sphere on which the asymptotic form of the magnetic field changes, and the second from r_1 to r_0, where r_0 is the radial value of the flow of line under consideration for $\theta = \pi/2$. This implies that the following expansions only apply to small impact parameters p with $r_0 \le r_1$. By expanding the integrand of (A17) in powers of $1/r$ for $r > r_1 > R$ and in the region $0 \le \theta \le \pi/2$, we determine $C_1 = 0$ and we recover the homogeneous field at infinity with an accuracy to $O(1/r)$. Near the surface $r_1 > r > r_0$ we perform a change of the variable to $s = r - R$. We define $s_1 = r_1 - R$ and $s_0 = r_0 - R$ and s varies within $s_0 < s < s_1$. The equation of the line of flow (A3) has the form $p = \sqrt{3sR} \sin \theta$ with an accuracy to $O(s^{3/2})$ and from this we obtain $s_0 = p^2/(3R)$ for $\theta = \pi/2$ and $s = s_0$.

The value of B_r in this region will be composed of two terms: the value of the integral in (A17) from ∞ to r_1 with a factor to leading order $\propto s^{3/2}$, and the value of the integral from s_1 to s, which behaves like $O(s^{1/2})$. Neglecting the first term in comparison with the second, we obtain for B_r with an accuracy to $O(s^{3/2})$ or $O(p^3)$:

$$B_r = -\frac{3s}{R} B_0 \, p \sin \phi \cos \theta \int_{s_1}^{s} \frac{s \, \mathrm{d}s}{9 \, (s^2 - ss_0)^{3/2}}. \tag{A19}$$

For impact parameters p with $s_0 \le s_1$, we obtain with an accuracy to $O(s_0/s_1)$:

$$B_r = \frac{2}{3} B_0 \sqrt{\frac{3s}{R}} \frac{\sin \theta}{1 + \cos \theta} \sin \phi. \tag{A20}$$

Using Eqn. (A14) leads to the component B_θ. Thus, B_θ and B_ϕ near the sphere are determined by the formulae

$$B_\theta = B_0 \sin \phi \, \sqrt{\frac{R}{3s}}, \tag{A21}$$

$$B_\phi = B_0 \cos \phi \, \sqrt{\frac{R}{3s}}. \tag{A22}$$

It turns out that these formulae are also correct for the region $\pi/2 \le \theta \le \pi$ as follows from Eqn. (A18). The integral in this expression is regular for s_0, and by computing B_θ in the approximation $s \ll R$ for $s = s_0$, we find $C_2 = \sin \phi \, R \, B_0/3$. Then B_θ is equal to (A21) with an accuracy to terms of order $O(s^{1/2})$. We obtain (A22) by using (A14). Thus, Eqns. (A20) to (A22) uniformly describe the field near the sphere with respect to the angle θ.

In order to facilitate comparison to our numerical solution, we transform the approximate solution for B given by the components in the spherical coordinate system (A20) to (A22) into

Cartesian system yielding

$$B_x = B_0 \cos\phi \sin\phi \, (1 - \cos\theta) \sqrt{\frac{R}{3s}} \left(\frac{2s}{R} - 1\right), \tag{A23}$$

$$B_y = B_0 \sqrt{\frac{R}{3s}} \left[\sin^2\phi \, (1 - \cos\theta) \left(\frac{2s}{R} - 1\right) + 1\right] = B_x \tan\phi + B_0 \sqrt{\frac{R}{3s}}, \tag{A24}$$

$$B_z = B_0 \sin\phi \sin\theta \sqrt{\frac{R}{3s}} \left(\frac{2s}{R} \frac{\cos\theta}{1 + \cos\theta} - 1\right). \tag{A25}$$

Note that we introduced the radial coordinate from the surface of the sphere $s = r - R$ and that this solution applies only near the sphere with an accuracy to $O(s^{3/2})$ as well as for small impact parameters p with an accuracy to $O(s_0/s_1)$.

Using the method of regularization of the integral in (A17) with respect to the lower limit $\theta = \pi/2$, Bernikov and Semenov (1980) investigate the behavior of the magnetic field in the wake of the sphere. They find that, when neglecting a term that scales as $O(1/r)$, B_r is given by

$$B_r = \frac{4}{3} \frac{B_0 \sin\phi}{p}, \tag{A26}$$

which, with proximity to the axis of the wake $p \to 0$, leads to an unlimited increase of $B_r \to \infty$. The magnetic lines of force that end at the stagnation point are strongly elongated as the swipe around the sphere parallel to the line of flow reaching from the stagnation point into the rear. This leads to the unphysical increase of the magnetic field as it approaches the symmetry line. While this might be the mathematically correct solution, it leads to a logarithmic divergence of the energy density of the magnetic field in the volume near the wall.

REFERENCES

N. Asai, N. Fukuda, and R. Matsumoto. MHD Simulations of a Moving Subclump with Heat Conduction. *Journal of Korean Astronomical Society*, 37:575–578, December 2004.

N. Asai, N. Fukuda, and R. Matsumoto. Three-dimensional MHD simulations of X-ray emitting subcluster plasmas in cluster of galaxies. *Advances in Space Research*, 36:636–642, 2005. doi: 10.1016/j.asr.2005.04.041.

N. Asai, N. Fukuda, and R. Matsumoto. MHD simulations of plasma heating in clusters of galaxies. *Astronomische Nachrichten*, 327:605–+, June 2006. doi: 10.1002/asna.200610601.

D. G. Barnes and C. J. Fluke. Incorporating interactive 3-dimensional graphics in astronomy research papers. *ArXiv e-prints*, 709, September 2007.

L. V. Bernikov and V. S. Semenov. Problem of MHD flow around the magnetosphere. *Geomagnetizm i Aeronomiia*, 19:671–675, February 1980.

L. Bîrzan, D. A. Rafferty, B. R. McNamara, M. W. Wise, and P. E. J. Nulsen. A Systematic Study of Radio-induced X-Ray Cavities in Clusters, Groups, and Galaxies. *ApJ*, 607:800–809, June 2004. doi: 10.1086/383519.

M. Brüggen. Simulations of Buoyant Bubbles in Galaxy Clusters. *ApJ*, 592:839–845, August 2003. doi: 10.1086/375731.

M. Brüggen and C. R. Kaiser. Hot bubbles from active galactic nuclei as a heat source in cooling-flow clusters. *Nature*, 418:301–303, July 2002.

A. C. Calder, B. Fryxell, T. Plewa, R. Rosner, L. J. Dursi, V. G. Weirs, T. Dupont, H. F. Robey, J. O. Kane, B. A. Remington, R. P. Drake, G. Dimonte, M. Zingale, F. X. Timmes, K. Olson, P. Ricker, P. MacNeice, and H. M. Tufo. On Validating an Astrophysical Simulation Code. *ApJS*, 143:201–229, November 2002. doi: 10.1086/342267.

S. Chandrasekhar. *Hydrodynamic and Hydromagnetic Stability*. Dover, New York, 1981.

C. Dalla Vecchia, R. G. Bower, T. Theuns, M. L. Balogh, P. Mazzotta, and C. S. Frenk. Quenching cluster cooling flows with recurrent hot plasma bubbles. *MNRAS*, 355:995–1004, December 2004. doi: 10.1111/j.1365-2966.2004.08381.x.

L. J. Dursi. Bubble-Wrap for Bullets: The Stability Imparted By A Thin Magnetic Layer. *Astrophysical Journal*, 670:221, November 2007.

S. Ettori and A. C. Fabian. Chandra constraints on the thermal conduction in the intracluster plasma of A2142. *MNRAS*, 317:L57–L59, September 2000.

B. Fryxell, K. Olson, P. Ricker, F. X. Timmes, M. Zingale, D. Q. Lamb, P. MacNeice, R. Rosner, J. W. Truran, and H. Tufo. FLASH: An Adaptive Mesh Hydrodynamics Code for Modeling Astrophysical Thermonuclear Flashes. *ApJS*, 131:273–334, November 2000. doi: 10.1086/ 317361.

A. Gardini. Buoyant Bubbles in a Cooling Intracluster Medium I. Hydrodynamic Bubbles. *ArXiv Astrophysics e-prints*, pages 11444–+, November 2006.

S. Heinz, E. Churazov, W. Forman, C. Jones, and U. G. Briel. Ram pressure stripping and the formation of cold fronts. *MNRAS*, 346:13–17, November 2003. doi: 10.1046/j.1365-2966. 2003.07066.x.

S. Heinz, M. Brüggen, A. Young, and E. Levesque. The answer is blowing in the wind: simulating the interaction of jets with dynamic cluster atmospheres. *MNRAS*, 373:L65–L69, November 2006. doi: 10.1111/j.1745-3933.2006.00243.x.

N. J. Kotschin, I. A. Kibel, and N. W. Rose. *Theoretische Hydrodynamik, Band 1*. Akademie Verlag, Berlin, 1954.

L. D. Landau and E. M. Lifshitz. *Fluid mechanics*. Butterworth-Heinemann, 2nd edition, 1987.

M. Lyutikov. Dissipation in Intercluster Plasma. *ApJ*, 668:L1–L4, October 2007. doi: 10.1086/ 522696.

M. Lyutikov. Magnetic draping of merging cores and radio bubbles in clusters of galaxies. *MNRAS*, 373:73–78, November 2006. doi: 10.1111/j.1365-2966.2006.10835.x.

M. Markevitch and A. Vikhlinin. Shocks and cold fronts in galaxy clusters. *Phys. Rep.*, 443:1–53, May 2007. doi: 10.1016/j.physrep.2007.01.001.

B. R. McNamara, P. E. J. Nulsen, M. W. Wise, D. A. Rafferty, C. Carilli, C. L. Sarazin, and E. L. Blanton. The heating of gas in a galaxy cluster by X-ray cavities and large-scale shock fronts. *Nature*, 433:45–47, January 2005. doi: 10.1038/nature03202.

G. Pavlovski, C. R. Kaiser, and E. C. D. Pope. Dynamics of buoyant bubbles in clusters of galaxies. *ArXiv e-prints*, 709, September 2007.

E. C. D. Pope, G. Pavlovski, C. R. Kaiser, and H. Fangohr. The effects of thermal conduction on the intracluster medium of the Virgo cluster. *MNRAS*, 364:13–28, November 2005. doi: 10.1111/j.1365-2966.2005.09449.x.

K. G. Powell, P. L. Roe, T. J. Linde, T. I. Gombosi, and D. L. de Zeeuw. A Solution-Adaptive Upwind Scheme for Ideal Magnetohydrodynamics. *Journal of Computational Physics*, 154:284–309, September 1999.

K. Robinson, L. J. Dursi, P. M. Ricker, R. Rosner, A. C. Calder, M. Zingale, J. W. Truran, T. Linde, A. Caceres, B. Fryxell, K. Olson, K. Riley, A. Siegel, and N. Vladimirova. Morphology of Rising Hydrodynamic and Magnetohydrodynamic Bubbles from Numerical Simulations. *ApJ*, 601:621–643, February 2004. doi: 10.1086/380817.

E. Roediger, M. Brueggen, P. Rebusco, H. Boehringer, and E. Churazov. Metal mixing by buoyant bubbles in galaxy clusters. *ArXiv Astrophysics e-prints*, pages 11531–+, November 2006.

M. Ruszkowski, T. A. Ensslin, M. Bruggen, M. C. Begelman, and E. Churazov. Cosmic ray confinement in fossil cluster bubbles. *ArXiv e-prints*, 705, May 2007a.

M. Ruszkowski, T. A. Enßlin, M. Brüggen, S. Heinz, and C. Pfrommer. Impact of tangled magnetic fields on fossil radio bubbles. *MNRAS*, pages 400–+, May 2007b. doi: 10.1111/j.1365-2966.2007.11801.x.

A. A. Schekochihin, S. C. Cowley, W. Dorland, G. W. Hammett, G. G. Howes, E. Quataert, and T. Tatsuno. Kinetic and fluid turbulent cascades in magnetized weakly collisional astrophysical plasmas. *ArXiv e-prints*, 704, March 2007.

A. Vikhlinin, M. Markevitch, and S. S. Murray. A Moving Cold Front in the Intergalactic Medium of A3667. *ApJ*, 551:160–171, April 2001. doi: 10.1086/320078.